

RESEARCH ARTICLE

Analysis and comparison of boundary condition variants in the free-surface lattice Boltzmann method

Christoph Schwarzmeier*¹ | Ulrich Rüde^{1,2}

¹Chair for System Simulation, Friedrich-Alexander-Universität Erlangen-Nürnberg, Cauerstraße 11, 91058 Erlangen, Germany

²CERFACS, 42 Avenue Gaspard Coriolis, 31057 Toulouse Cedex 1, France

Correspondence

*Christoph Schwarzmeier, Chair for System Simulation, Friedrich-Alexander-Universität Erlangen-Nürnberg, Cauerstraße 11, 91058 Erlangen, Germany.

Email: christoph.schwarzmeier@fau.de

Present Address

Chair for System Simulation, Friedrich-Alexander-Universität Erlangen-Nürnberg, Cauerstraße 11, 91058 Erlangen, Germany

Summary

The accuracy of the free-surface lattice Boltzmann method (FSLBM) depends significantly on the boundary condition employed at the free interface. Ideally, the chosen boundary condition balances the forces exerted by the liquid and gas pressure. Different variants of the same boundary condition are possible, depending on the number and choice of the particle distribution functions (PDFs) to which it is applied. This study analyzes and compares four variants, in which (i) the boundary condition is applied to all PDFs oriented in the opposite direction of the free interface's normal vector, including or (ii) excluding the central PDF. While these variants overwrite existing information, the boundary condition can also be applied (iii) to only missing PDFs without dropping available data or (iv) to only missing PDFs but at least three PDFs as suggested in the literature. It is shown that neither variant generally balances the forces exerted by the liquid and gas pressure at the free surface. The four variants' accuracy was compared in five different numerical experiments covering various applications. These include a standing gravity wave, a rectangular and cylindrical dam break, a rising Taylor bubble, and a droplet impacting a thin pool of liquid. Overall, variant (iii) was substantially more accurate than the other variants in the numerical experiments performed in this study.

KEYWORDS:

lattice Boltzmann method, free-surface flow, free-surface boundary condition, gravity wave, dam break, Taylor bubble

1 | INTRODUCTION

The free-surface lattice Boltzmann method (FSLBM)¹ is a well-established approach for simulating free-surface flows with the lattice Boltzmann method (LBM). In this context, *free-surface flow* refers to an immiscible two-fluid flow problem, the flow dynamics of which are assumed to be entirely governed by the heavier fluid. Consequently, the flow dynamics of the lighter fluid are neglected such that the problem reduces to a single-fluid flow with a free boundary². The free boundary, that is, the interface, is tracked according to the volume-of-fluid (VOF) approach³. There, an indicator denotes the affiliation to one of the fluids. In this article, the lighter fluid is called gas phase, and the heavier fluid is referred to as the liquid phase. The FSLBM has been successfully validated in simulations of different applications, including rising bubbles⁴, waves⁵, dam break scenarios⁶, drop impacts⁷ and electron-beam melting⁸.

There are other multiphase LBM models available in the literature. Models such as the FSLBM, the level-set method⁹, the front-tracking approach¹⁰, and the color gradient model¹¹ represent the interface between the fluids in a sharp manner. This is in contrast to models with a diffuse interface, such as phase-field models^{12,13,14}, the free-energy model¹⁵, and the pseudopotential model¹⁶. Sharp interface models generally require a lower computational resolution than models with a diffuse interface. Despite this advantage in computational efficiency, the FSLBM is also inherently applicable to systems with (infinitely) large density and viscosity ratios. However, the FSLBM can not be applied when the flow in the lighter fluid is relevant for the system's dynamics. Additionally, the FSLBM's algorithm is relatively complicated when compared to phase-field models, for example. More details on the FSLBM's advantages and disadvantages, and a comparison with an Allen–Cahn LBM phase-field model are presented in prior work¹⁷.

In the LBM, each cell of the computational grid contains particle distribution functions (PDFs), which represent the flow field information. In every simulation time step, these PDFs stream to all cells in their direct surrounding. Since the flow dynamics of the lighter phase are neglected in the FSLBM, gas cells do not carry valid PDF information. Therefore, PDFs streaming from the gas towards the liquid phase are unavailable. They must be reconstructed using a boundary condition for the free surface. In the original FSLBM introduced by Körner et al.¹, the suggested boundary condition is not only applied to reconstruct missing PDFs. Instead, it is applied so that existing PDFs from the liquid phase are also reconstructed. Consequently, available information about the flow field is dropped. Körner et al. argue that this is required to balance the forces exerted by the liquid and gas at the interface. However, other authors have reported anisotropic artifacts¹⁸ or implausible simulation results⁵ when available information is overwritten by the boundary condition. This article will show that the force-balance computation from Körner et al.¹ must be corrected, as forces are only balanced in steady-state systems but not generally. In the study presented here, other variants of applying the free boundary condition are analyzed, compared, and found to be more accurate than that from Körner et al.¹

In the first section, the numerical foundations of the LBM and FSLBM are introduced. Then, the balance of forces at the interface is computed for four different variants of applying the free-surface boundary condition. These include the variant by Körner et al.¹, where PDFs are reconstructed based on the orientation of the interface-normal. In this variant, existing PDFs are overwritten. While not explicitly mentioned in the article¹, the central PDF must also be reconstructed in this variant. The second variant under investigation is similar to the first one. However, the central PDF is not overwritten. In the third variant, only missing PDFs are reconstructed. Therefore, no existing fluid flow information is dropped. In the final variant, only missing but at least three PDFs are reconstructed^{19,20}. The force-balance computations show that neither of these four variants generally balances the forces at the interface. In five different numerical experiments, the boundary condition variants are then compared in different applications. These include a standing gravity wave, a rectangular and cylindrical dam break, the rise of a Taylor bubble, and the formation of the splash crown when a drop impacts a pool of liquid. Finally, it is concluded that it is preferable to avoid overwriting existing information. Instead, only missing PDFs should be reconstructed with the free-surface boundary condition.

The source code of the implementation used in this study is freely available as part of the open source C++ software framework WALBERLA²¹ (<https://www.walberla.net>). The version of walBerla used in this article is provided in the supporting information.

2 | NUMERICAL METHODS

This section introduces the numerical foundations of the lattice Boltzmann method and its extension to free-surface flows, the free-surface lattice Boltzmann method. The section is based on Section 2 in articles^{17,22} but is repeated here for completeness.

2.1 | Lattice Boltzmann method

The lattice Boltzmann method is a relatively modern approach for simulating computational fluid dynamics. A thorough introduction to the LBM is available in the literature²³. Here, only its fundamental aspects are introduced.

The LBM discretizes the Boltzmann equation from kinetic gas theory and describes the evolution of particle distribution functions on a uniformly discretized Cartesian lattice with spacing $\Delta x \in \mathbb{R}^+$. In each lattice cell, the macroscopic fluid velocity is discretized with the $DdQq$ velocity set, where $d \in \mathbb{N}$ refers to the lattice's spatial dimension and $q \in \mathbb{N}$ refers to the number of PDFs per cell. A PDF $f_i(\mathbf{x}, t) \in \mathbb{R}$ with $i \in \{0, 1, \dots, q-1\}$ represents the probability that there exists a population of virtual fluid particles at time $t \in \mathbb{R}^+$ and position $\mathbf{x} \in \mathbb{R}^d$ traveling with lattice velocity $\mathbf{c}_i \in \Delta x / \Delta t \{-1, 0, 1\}^d$. The time is discretized by distinct time steps of length Δt . The discrete lattice Boltzmann equation can be written in the subsequent steps of collision,

also called relaxation,

$$f_i^*(\mathbf{x}, t) = f_i(\mathbf{x}, t) + \Omega_i(\mathbf{x}, t) + F_i(\mathbf{x}, t) \quad (1)$$

and streaming, also called propagation,

$$f_i(\mathbf{x} + \mathbf{c}_i \Delta t, t + \Delta t) = f_i^*(\mathbf{x}, t). \quad (2)$$

In the collision step, the collision operator $\Omega_i(\mathbf{x}, t) \in \mathbb{R}$ relaxes the PDFs towards an equilibrium state $f_i^{\text{eq}}(\mathbf{x}, t)$ while being influenced by external forces $F_i(\mathbf{x}, t) \in \mathbb{R}$. In the streaming step, the post-collision PDFs $f_i^*(\mathbf{x}, t)$ stream to neighboring cells. In the present article, the single relaxation time (SRT) collision operator

$$\Omega_i(\mathbf{x}, t) = \frac{f_i(\mathbf{x}, t) - f_i^{\text{eq}}(\mathbf{x}, t)}{\tau} \Delta t \quad (3)$$

is used with relaxation time $\tau > \Delta t/2$. The PDF's equilibrium can be derived from the continuous Maxwell–Boltzmann distribution²⁴ and is given by

$$f_i^{\text{eq}}(\mathbf{x}, t) = w_i \rho \left(1 + \frac{\mathbf{u} \cdot \mathbf{c}_i}{c_s^2} + \frac{(\mathbf{u} \cdot \mathbf{c}_i)^2}{2c_s^4} - \frac{\mathbf{u} \cdot \mathbf{u}}{2c_s^2} \right). \quad (4)$$

It includes the lattice weights $w_i \in \mathbb{R}$, the lattice speed of sound c_s^2 , the macroscopic fluid density $\rho \equiv \rho(\mathbf{x}, t) \in \mathbb{R}^+$, and the macroscopic fluid velocity $\mathbf{u} \equiv \mathbf{u}(\mathbf{x}, t) \in \mathbb{R}^d$. In this study, the well-established D2Q9 and D3Q19 lattice models are used. The corresponding lattice weights can be found in the literature²³. The lattice speed of sound $c_s^2 = \sqrt{1/3} \Delta x / \Delta t$ defines the relation between the macroscopic fluid density $\rho(\mathbf{x}, t)$ and pressure $p(\mathbf{x}, t) = c_s^2 \rho(\mathbf{x}, t)$. The PDFs' zeroth-order moment is the density

$$\rho(\mathbf{x}, t) = \sum_i f_i(\mathbf{x}, t) \quad (5)$$

and the first-order moment reveals the macroscopic fluid velocity

$$\mathbf{u}(\mathbf{x}, t) = \frac{\mathbf{F}(\mathbf{x}, t) \Delta t}{2\rho(\mathbf{x}, t)} + \frac{1}{\rho(\mathbf{x}, t)} \sum_i \mathbf{c}_i f_i(\mathbf{x}, t), \quad (6)$$

where $\mathbf{F}(\mathbf{x}, t) \in \mathbb{R}^d$ is an external force. The fluid's kinematic viscosity

$$\nu = c_s^2 \left(\tau - \frac{\Delta t}{2} \right) \quad (7)$$

can be computed from the relaxation time τ , that is, relaxation rate $\omega = 1/\tau$. In this article, the gravitational force, as part of F_i in the LBM collision (1), was modeled according to Guo et al.²⁵ with

$$F_i(\mathbf{x}, t) = \left(1 - \frac{\Delta t}{2\tau} \right) w_i \left(\frac{\mathbf{c}_i - \mathbf{u}}{c_s^2} + \frac{(\mathbf{c}_i \cdot \mathbf{u}) \mathbf{c}_i}{c_s^4} \right) \cdot \mathbf{F}(\mathbf{x}, t), \quad (8)$$

where $\mathbf{u} \equiv \mathbf{u}(\mathbf{x}, t)$ was used as before.

For the simulations of the rectangular and cylindrical dam break in Sections 4.2 and 4.3, a Smagorinsky-type large eddy simulation turbulence model was employed^{26,27}. With the user-chosen relaxation time $\tau_0 > \Delta t/2$, the model locally adjusts the collision operator's relaxation time $\tau(\mathbf{x}, t) = \tau_0 + \tau_t(\mathbf{x}, t)$ with a contribution $\tau_t(\mathbf{x}, t) \in \mathbb{R}$ from the turbulence viscosity

$$\nu_t(\mathbf{x}, t) := \tau_t(\mathbf{x}, t) c_s^2 = (C_S \Delta x_{\text{LES}})^2 \bar{S}(\mathbf{x}, t), \quad (9)$$

where Δx_{LES} is the filter length, C_S is the Smagorinsky constant, and

$$\bar{S}(\mathbf{x}, t) = \frac{\bar{Q}(\mathbf{x}, t)}{2\rho c_s^2 \tau_0} \quad (10)$$

is the filtered strain rate tensor. The filtered mean momentum flux

$$\bar{Q}(\mathbf{x}, t) = \sqrt{2 \sum_{\alpha, \beta} \bar{Q}_{\alpha, \beta}(\mathbf{x}, t) \bar{Q}_{\alpha, \beta}(\mathbf{x}, t)} \quad (11)$$

is computed from the momentum fluxes

$$\bar{Q}_{\alpha, \beta}(\mathbf{x}, t) = \sum_i c_{i, \alpha} c_{i, \beta} \left(f_i(\mathbf{x}, t) - f_i^{\text{eq}}(\mathbf{x}, t) \right) \quad (12)$$

as obtained from the second-order moments of the non-equilibrium parts of the PDFs. The indices α and β are used to refer to the components of a vector or tensor in index notation. The turbulence relaxation time is then given by²⁶

$$\tau_t(\mathbf{x}, t) = \frac{1}{2} \sqrt{\tau_0^2 + 2\sqrt{2}(C_S \Delta x_{\text{LES}})^2 (\rho c_s^4)^{-1} \bar{Q}(\mathbf{x}, t)} - \tau_0. \quad (13)$$

In the simulations performed in this article, $\Delta x_{\text{LES}} = \Delta x$ and $C_S = 0.1^{27}$ were chosen.

The bounce-back approach was used at solid obstacles with a no-slip boundary condition. In this approach, PDFs streaming into solid obstacle cells are reflected reversely, that is, their original direction with index i is reversed, denoted as \bar{i} , with lattice velocity $c_{\bar{i}} = -c_i^{23}$. Free-slip boundary conditions are realized similarly, with the PDFs being reflected specularly. Consequently, the normal velocity component of the incoming velocity c_i is reversed with $c_{j,n} = -c_{i,n}$, where c_j is the resulting lattice velocity²³.

As commonly used in the context of the LBM, $\Delta x = 1$ and $\Delta t = 1$ are chosen in the remainder of this article. Therefore, all quantities are denoted in the LBM unit system if not explicitly stated otherwise. In all simulations, the LBM reference density $\rho_0 = 1$ and pressure $p_0 = c_s^2 \rho_0 = 1/3$ were set. The relaxation times τ or relaxation rates ω specified for the numerical experiments refer to the constant user-chosen values that are not yet adjusted by the Smagorinsky turbulence model.

2.2 | Free-surface lattice Boltzmann method

The free-surface lattice Boltzmann method used in this article is based on the approach from Körner et al.¹ It simulates a moving interface between two immiscible fluids, the heavier of which completely governs the flow dynamics of the system. The immiscible two-fluid flow problem is therefore reduced to a single-fluid flow with a free boundary. In practice, this simplification is valid if the densities and viscosities of the fluids differ substantially, such as in liquid–gas flow. In the following, the heavier fluid is referred to as liquid, whereas the lighter fluid is referred to as gas.

The interface between the liquid and the gas is treated as in the volume-of-fluid approach³, where each lattice cell gets assigned a fill level $\varphi(\mathbf{x}, t)$. The fill level acts as an indicator describing the affiliation to one of the phases. Cells can either be of liquid ($\varphi(\mathbf{x}, t) = 1$), gas ($\varphi(\mathbf{x}, t) = 0$), or interface type ($\varphi(\mathbf{x}, t) \in (0, 1)$). The interface cells form a sharp and closed layer, which separates liquid and gas cells. Interface and liquid cells are treated as regular LBM cells that contain PDFs and participate in the LBM collision (1) and streaming (2). In contrast, agreeing with the free-surface assumption, gas cells neither contain PDFs nor participate in the LBM update.

The liquid mass of each cell

$$m(\mathbf{x}, t) = \varphi(\mathbf{x}, t) \rho(\mathbf{x}, t) \Delta x^3 \quad (14)$$

is determined by the cell's fill level $\varphi(\mathbf{x}, t)$, fluid density $\rho(\mathbf{x}, t)$, and volume Δx^3 . The mass flux between an interface cell and other cells is computed from the LBM streaming step via

$$\frac{\Delta m_i(\mathbf{x}, t)}{\Delta x^3} = \begin{cases} 0 & \mathbf{x} + c_i \Delta t \in \text{gas} \\ f_i^*(\mathbf{x} + c_i \Delta t, t) - f_i^*(\mathbf{x}, t) & \mathbf{x} + c_i \Delta t \in \text{liquid} \\ \frac{1}{2} \left(\varphi(\mathbf{x}, t) + \varphi(\mathbf{x} + c_i \Delta t, t) \right) \left(f_{\bar{i}}^*(\mathbf{x} + c_i \Delta t, t) - f_i^*(\mathbf{x}, t) \right) & \mathbf{x} + c_i \Delta t \in \text{interface,} \end{cases} \quad (15)$$

where \bar{i} denotes the inversion of the lattice direction, leading to $c_{\bar{i}} = -c_i$. Note that the fluid density $\rho(\mathbf{x}, t)$ is computed by the PDFs' zeroth-order moment (5), that is, by the PDFs' sum. Therefore, the PDFs' unit is the same as the macroscopic fluid density's unit, making Equations (14) and (15) consistent.

In the implementation used here, interface cells are not immediately converted to liquid or gas cells when they become full ($\varphi(\mathbf{x}, t) = 1$) or empty ($\varphi(\mathbf{x}, t) = 0$). Instead, the heuristically chosen threshold $\varepsilon_\varphi = 10^{-2}$ is used to prevent oscillatory conversions²⁸. Therefore, an interface cell converts to liquid or gas if $\varphi(\mathbf{x}, t) > 1 + \varepsilon_\varphi$ or $\varphi(\mathbf{x}, t) < 0 - \varepsilon_\varphi$. During such conversions, surrounding gas or liquid cells must be converted to interface cells to maintain a closed interface layer. It is important to note that neither liquid nor gas cells can directly convert into one another but only to interface cells. In case of conflicting conversions, the separation of liquid and gas is prioritized. When converting an interface cell with fill level $\varphi^{\text{conv}}(\mathbf{x}, t)$ to gas or liquid, the fill level is forcefully set to $\varphi(\mathbf{x}, t) = 0$ or $\varphi(\mathbf{x}, t) = 1$ to ensure consistency with the cell type definitions. This manual modification of the fill level may lead to small amounts of excessive mass $m_{\text{ex}}(\mathbf{x}, t)$ with

$$\frac{m_{\text{ex}}(\mathbf{x}, t)}{\rho(\mathbf{x}, t) \Delta x^3} = \begin{cases} \varphi^{\text{conv}}(\mathbf{x}, t) - 1 & \text{if } \mathbf{x} \text{ is converted to liquid} \\ \varphi^{\text{conv}}(\mathbf{x}, t) & \text{if } \mathbf{x} \text{ is converted to gas.} \end{cases} \quad (16)$$

This excess mass is distributed evenly among all interface cells in the neighborhood of the converted cell to conserve the system's total mass.

There may appear unnecessary interface cells without gas or liquid neighbors during a simulation. In the implementation used in this study, these cells are forced to fill or empty by adjusting the mass flux (15), as suggested by Thürey²⁹.

When converting cells from interface to liquid or vice-versa, the PDFs of the cell are not modified. In contrast, when converting interface cells to gas cells, the interface cells' PDFs are dropped. However, no valid PDFs are available when converting gas

cells to interface cells. The PDFs of these cells are initialized with their equilibrium (4) with $\rho(\mathbf{x}, t)$ and $\mathbf{u}(\mathbf{x}, t)$ averaged from all surrounding liquid and non-newly created interface cells.

The LBM collision (1) and streaming (2) is performed in all interface and liquid cells. As opposed to Körner et al.¹, following other authors^{19,28,30}, the gravitational force is not weighted with an interface cell's fill level in the LBM collision in this article.

The macroscopic boundary condition at the free surface is given by^{2,19}

$$\begin{aligned} p(\mathbf{x}, t) - p^G(\mathbf{x}, t) + p^L(\mathbf{x}, t) &= 2\mu\partial_n u_n(\mathbf{x}, t) \\ 0 &= \partial_{t_1} u_n(\mathbf{x}, t) + \partial_n u_{t_1}(\mathbf{x}, t) \\ 0 &= \partial_{t_2} u_n(\mathbf{x}, t) + \partial_n u_{t_2}(\mathbf{x}, t). \end{aligned} \quad (17)$$

It includes the gas pressure $p^G(\mathbf{x}, t)$, Laplace pressure $p^L(\mathbf{x}, t)$, tangent vectors $\mathbf{t}_1(\mathbf{x}, t) \in \mathbb{R}^d$ and $\mathbf{t}_2(\mathbf{x}, t) \in \mathbb{R}^d$, and normal vector $\mathbf{n}(\mathbf{x}, t)$. Körner et al.¹ suggested to use the LBM anti-bounce-back pressure boundary condition

$$f_i^*(\mathbf{x} - \mathbf{c}_i \Delta t, t) = f_i^{\text{eq}}(\rho^G, \mathbf{u}) + f_{\bar{i}}^{\text{eq}}(\rho^G, \mathbf{u}) - f_{\bar{i}}^*(\mathbf{x}, t) \quad (18)$$

at the free interface, with the interface cell's velocity $\mathbf{u} \equiv \mathbf{u}(\mathbf{x}, t)$ and gas density $\rho^G \equiv \rho^G(\mathbf{x}, t) = p^G(\mathbf{x}, t) / c_s^2$. Other formulations of the boundary condition have been investigated in the literature^{20,31}. The free-surface boundary condition (18) must be applied to all PDFs streaming from gas cells to interface cells as they are unavailable. However, Körner et al.¹ proposed to reconstruct not only missing PDFs but also available PDFs. Consequently, this approach drops existing flow-field information. The theoretical justification and evaluation for this suggestion are discussed in close detail in Section 3. Its implications are investigated in the numerical experiments in Section 4. At free-slip boundaries, the free-surface boundary condition (18) must also be applied to specularly reflected PDFs originating from gas cells.

The gas pressure

$$p^G(\mathbf{x}, t) = p^V(t) - p^L(\mathbf{x}, t) \quad (19)$$

incorporates the volume pressure $p^V(t)$ and the Laplace pressure $p^L(\mathbf{x}, t)$. The volume pressure can be assumed constant in case of atmospheric pressure or result from changes in the volume of an enclosed gas volume, that is, bubble, according to

$$p^V(t) = p^V(0) \frac{V(0)}{V(t)}. \quad (20)$$

The Laplace pressure

$$p^L(\mathbf{x}, t) = 2\sigma\kappa(\mathbf{x}, t) \quad (21)$$

is determined by the surface tension $\sigma \in \mathbb{R}^+$ and the interface curvature $\kappa(\mathbf{x}, t) \in \mathbb{R}$. In the simulations shown in this article, the interface curvature

$$\kappa(\mathbf{x}, t) = -\nabla \cdot \hat{\mathbf{n}}(\mathbf{x}, t) \quad (22)$$

was computed using the finite difference method (FDM) following Bogner et al.¹⁸ The normalized interface normal $\hat{\mathbf{n}}(\mathbf{x}, t) = \mathbf{n}(\mathbf{x}, t) / |\mathbf{n}(\mathbf{x}, t)|$ was obtained with a weighted central FDM according to Parker and Youngs³² of

$$\mathbf{n}(\mathbf{x}, t) = \nabla\varphi(\mathbf{x}, t). \quad (23)$$

The computation of $\mathbf{n}(\mathbf{x}, t) \in \mathbb{R}^d$ was modified near near solid obstacle cells according to Donath³⁰ so that the FDM's access pattern did not include obstacle cells. The curvature $\kappa(\mathbf{x}, t)$ is effectively computed from a second-order derivative of the fill level $\varphi(\mathbf{x}, t)$. Since $\varphi(\mathbf{x}, t)$ is a non-smooth indicator function, taking its second-order derivative introduces large errors. To reduce these errors, the fill level as used in the normal computation (23), is smoothed using the K_8 -Kernel from Reference³³ with a support radius of 2.0. A more detailed description of these steps, and a comparison with other curvature computation models is available in the work of Bogner et al.¹⁸ A bubble model algorithm is used to track the volume pressure of bubbles during coalescence or segmentation^{28,34}.

3 | FREE-SURFACE BOUNDARY CONDITION VARIANTS

As mentioned in the preceding section, gas cells do not contain PDFs. Therefore, PDFs propagating from gas to interface cells must be reconstructed in the LBM streaming step. The reconstruction must satisfy the free-surface boundary condition (17), balancing the forces exerted by the liquid and gas pressure. Following Körner et al.¹, the balance of the forces can be analyzed using an approach based on the momentum exchange method^{35,36}. Assuming that the total force is determined by the PDFs streaming through the interface during one time step, the total force $\mathbf{F} \equiv \mathbf{F}(\mathbf{x}, t) \in \mathbb{R}^d$ exerted by the fluid on a surface element

$\mathbf{n}(\mathbf{x}, t) \cdot A(\mathbf{x}, t)$ results from the momentum transported by the particles streaming through this element. With the interface-normal $\mathbf{n} \equiv \mathbf{n}(\mathbf{x}, t) \in \mathbb{R}^d$ and surface area $A \equiv A(\mathbf{x}, t) \in \mathbb{R}$ the force is given by

$$\frac{F_\alpha}{A} = -n_\beta \left(\sum_{i \in K} f_i^*(\mathbf{x}, t)(c_{i,\alpha} - u_\alpha)(c_{i,\beta} - u_\beta) + \sum_{i \in R} f_i^*(\mathbf{x} - \mathbf{c}_i \Delta t, t)(c_{i,\alpha} - u_\alpha)(c_{i,\beta} - u_\beta) \right). \quad (24)$$

The macroscopic fluid velocity $\mathbf{u} \equiv \mathbf{u}(\mathbf{x}, t)$ is subtracted from the discrete lattice velocity \mathbf{c}_i to satisfy Galilean invariance, making the analysis independent of the frame of reference. Whereas PDFs contained in the first sum with $i \in K$ (*keep*) are not modified, PDFs included in the second sum with $i \in R$ (*reconstruct*) are reconstructed with the free-surface boundary condition (18).

The forces at the interface are balanced if the force exerted from the liquid is equal to the force from the gas pressure $p^G \equiv p^G(\mathbf{x}, t) \in \mathbb{R}$, as denoted by

$$\frac{F_\alpha}{A} \stackrel{!}{=} -n_\alpha p^G. \quad (25)$$

In the following four sections, the force balance for different definitions of K and R is computed. The name of each section refers to the PDFs that are reconstructed in the respective variant.

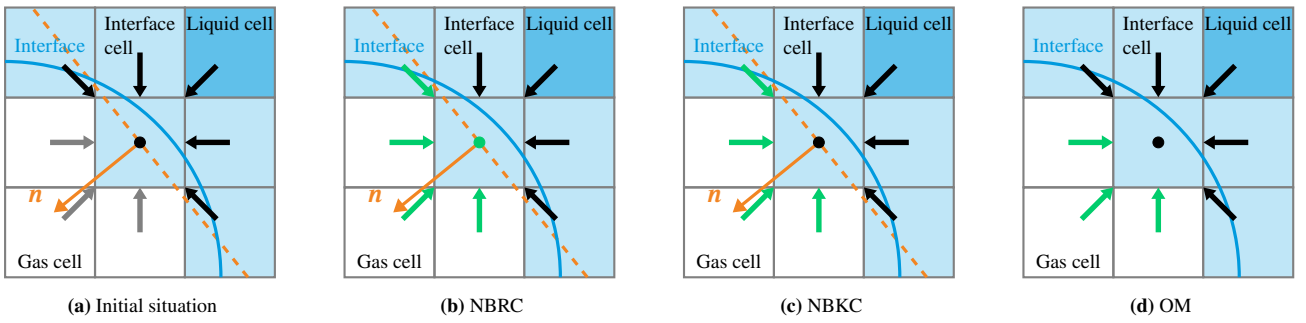


FIGURE 1 PDFs, visualized as arrows, stream into neighboring lattice cells (a) in the LBM streaming step. PDFs originating in liquid or interface cells are already available and displayed in black, whereas PDFs coming from gas cells must be reconstructed and are marked in gray. The PDFs reconstructed by the NBRC (b), NBKC (c) and OM (d) variants are colored in green. In the OM3 variant, at least three PDFs must be reconstructed. In the example here, this case is identical to the OM variant.

3.1 | Normal-based, reconstruct center (NBRC)

In the variant suggested in the original FSLBM model by Körner et al.¹, the PDFs are reconstructed based on the orientation of the interface-normal \mathbf{n} with

$$\begin{aligned} K & := \{i | \mathbf{n} \cdot \mathbf{c}_i < 0\} \\ R & := \{i | \mathbf{n} \cdot \mathbf{c}_i \geq 0\}. \end{aligned} \quad (26)$$

The authors¹ did not explicitly specify whether the central PDF f_0 must be reconstructed. However, formally, $\mathbf{c}_0 = 0$, so that it is included in R , the set of PDFs to be reconstructed. Therefore, this variant is referred to as *normal-based, reconstruct center* (NBRC) in this article.

Note that although $\mathbf{c}_0 = 0$, the respective summand in the force-balance equation is not generally zero because of the subtraction with the velocity \mathbf{u} . As illustrated in Figure 1b, the NBRC variant overwrites existing PDFs, that is, it drops available information. Körner et al.¹ argue that this is required to maintain the balance of forces at the interface. However, the central PDF is ignored in the force-balance computation in their article¹. Therefore, the forces are not generally balanced. The corrected force balance is given by

$$\begin{aligned} \frac{F_\alpha}{A} & = -n_\beta \left(\sum_{i \in \{i | \mathbf{n} \cdot \mathbf{c}_i < 0\}} f_i^*(\mathbf{x}, t)(c_{i,\alpha} - u_\alpha)(c_{i,\beta} - u_\beta) + \sum_{i \in \{i | \mathbf{n} \cdot \mathbf{c}_i \geq 0\}} f_i^*(\mathbf{x} - \mathbf{c}_i \Delta t, t)(c_{i,\alpha} - u_\alpha)(c_{i,\beta} - u_\beta) \right) \\ & = -n_\alpha p^G \\ & \quad + n_\beta \left(f_0^*(\mathbf{x}, t) - f_0^{\text{eq}}(\rho^G, \mathbf{u}) \right) u_\alpha u_\beta + 2n_\beta \sum_{i \in \{i | \mathbf{n} \cdot \mathbf{c}_i < 0\}} \left(f_i^*(\mathbf{x}, t) - f_i^{\text{eq}}(\rho^G, \mathbf{u}) \right) (c_{i,\alpha} u_\beta + c_{i,\beta} u_\alpha), \end{aligned} \quad (27)$$

where terms marked in orange are deviations from the desired balance of the forces. This result shows that no general estimate of the error can be made. The error depends on several non-constant quantities changing in time t and location \mathbf{x} in the simulation. These quantities include the macroscopic velocity $\mathbf{u}(\mathbf{x}, t)$, the interface-normal $\mathbf{n}(\mathbf{x}, t)$, the gas density $\rho^G(\mathbf{x}, t)$, and the specific values of the post-collision PDFs $f_i^*(\mathbf{x}, t)$. The forces at the interface are only guaranteed to be balanced if the interface cell is at a steady-state with $\mathbf{u}(\mathbf{x}, t) = \mathbf{0}$.

A step-by-step force-balance computation leading to the result in Equation (27) is available in Appendix A.1.

3.2 | Normal-based, keep center (NBKC)

In the *normal-based, keep-center* (NBKC) variant, visualized in Figure 1c, the central PDF f_0 is not modified. The sets K and R are then defined by

$$\begin{aligned} K & := \{i | \mathbf{n} \cdot \mathbf{c}_i < 0\} \\ R & := \{i | \mathbf{n} \cdot \mathbf{c}_i > 0\}. \end{aligned} \quad (28)$$

The force-balance computation gives

$$\begin{aligned} \frac{F_\alpha}{A} & = -n_\beta \left(\sum_{i \in \{i | \mathbf{n} \cdot \mathbf{c}_i < 0\}} f_i^*(\mathbf{x}, t) (c_{i,\alpha} - u_\alpha) (c_{i,\beta} - u_\beta) + \sum_{i \in \{i | \mathbf{n} \cdot \mathbf{c}_i > 0\}} f_i^*(\mathbf{x} - \mathbf{c}_i \Delta t, t) (c_{i,\alpha} - u_\alpha) (c_{i,\beta} - u_\beta) \right) \\ & = -n_\alpha p^G \\ & \quad + n_\beta f_0^{\text{eq}}(\rho^G, \mathbf{u}) u_\alpha u_\beta + 2n_\beta \sum_{i \in \{i | \mathbf{n} \cdot \mathbf{c}_i < 0\}} \left(f_i^*(\mathbf{x}, t) - f_i^{\text{eq}}(\rho^G, \mathbf{u}) \right) (c_{i,\alpha} u_\beta + c_{i,\beta} u_\alpha). \end{aligned} \quad (29)$$

where the terms marked in orange disturb the balance of the forces. As for the NBRC in Section 3.1, no general estimate about the error in the force balance can be made. The sole exception are steady-state interface cells with $\mathbf{u}(\mathbf{x}, t) = \mathbf{0}$, where the forces are guaranteed to be balanced.

Appendix A.2 presents the detailed force-balance computation that led to the result in Equation (29).

3.3 | Only missing (OM)

In the literature, authors have noticed issues when reconstructing missing PDFs based on the orientation of the interface-normal as proposed by Körner et al¹. These issues include anisotropic artifacts¹⁸ and the inability to model water wave propagation accurately⁵. However, neither reference explicitly specifies if the center PDF was reconstructed. Therefore, it remains unclear whether these issues were observed with the NBRC or NBKC variant.

The normal-based variants overwrite existing PDFs and do not generally balance the forces at the interface. Therefore, an obvious alternative is to reconstruct only missing PDFs (OM), as in Figure 1d, without discarding any flow field information. While this variant's balance of forces has not been analyzed theoretically in the literature, several authors^{6,18,37,38,39,40,41,42,43} have used it without further reasoning.

The sets K and R are defined by

$$\begin{aligned} K & \equiv N^- := \{i | \mathbf{x} - \mathbf{c}_i \Delta t \in \text{non-gas}\} \\ N^+ & := \{i | \mathbf{x} + \mathbf{c}_i \Delta t \in \text{non-gas}\} \\ R & \equiv G^- := \{i | \mathbf{x} - \mathbf{c}_i \Delta t \in \text{gas}\} \\ G^+ & := \{i | \mathbf{x} + \mathbf{c}_i \Delta t \in \text{gas}\} \\ T & := \{0, 1, \dots, q-1\} \end{aligned} \quad (30)$$

with the set T (*total*) containing all of a cell's PDFs. The expression $\mathbf{x} - \mathbf{c}_i \Delta t$ denotes that a PDF streams from a neighboring cell to the current cell. In contrast, a PDF with $\mathbf{x} + \mathbf{c}_i \Delta t$ streams from the current cell to a neighboring cell. Therefore, conforming with the free-surface boundary condition (18) and general force-balance computation (24), only PDFs streaming from a neighboring gas cell to this cell with $i \in G^-$ are reconstructed. Note that the sets are related by

$$\begin{aligned} i \in N^- & \Leftrightarrow \bar{i} \in N^+ \\ i \in G^- & \Leftrightarrow \bar{i} \in G^+. \end{aligned} \quad (31)$$

An index i is not exclusively in only one set but can be part of N^- and N^+ , or G^- and G^+ . The central PDF f_0 with $i = 0$ belongs to the interface cell itself and will always be a non-gas cell with $i = 0 \in N^-$ and $i = 0 \in N^+$ such that

$$G^- \cup N^- = T \quad (32)$$

$$G^+ \cup N^+ = T. \quad (33)$$

The force balance is then given by

$$\begin{aligned} \frac{F_\alpha}{A} &= -n_\beta \left(\sum_{i \in N^-} f_i^*(\mathbf{x}, t)(c_{i,\alpha} - u_\alpha)(c_{i,\beta} - u_\beta) + \sum_{i \in G^-} f_i^*(\mathbf{x} - \mathbf{c}_i \Delta t, t)(c_{i,\alpha} - u_\alpha)(c_{i,\beta} - u_\beta) \right) \\ &= -n_\alpha p^G \\ &\quad - n_\beta \sum_{i \in N^-} f_i^*(\mathbf{x}, t)(c_{i,\alpha} c_{i,\beta} - c_{i,\alpha} u_\beta - c_{i,\beta} u_\alpha + u_\alpha u_\beta) + n_\beta \sum_{i \in G^+} f_i^*(\mathbf{x}, t)(c_{i,\alpha} c_{i,\beta} + c_{i,\alpha} u_\beta + c_{i,\beta} u_\alpha + u_\alpha u_\beta) \\ &\quad + n_\beta \sum_{i \in T \setminus (G^- \cup G^+)} f_i^{\text{eq}}(\rho^G, \mathbf{u})(c_{i,\alpha} c_{i,\beta} - c_{i,\alpha} u_\beta - c_{i,\beta} u_\alpha + u_\alpha u_\beta) - 2n_\beta \sum_{i \in G^+} f_i^{\text{eq}}(\rho^G, \mathbf{u})(c_{i,\alpha} u_\beta + c_{i,\beta} u_\alpha), \end{aligned} \quad (34)$$

where the terms disturbing the force balance are marked in orange. As for the NBRC and NBKC variant, it is impossible to predict the error made in the force-balance computation generally. However, in contrast to the normal-based variants, the OM variant does not guarantee the balance of the forces at a steady-state interface.

The detailed step-by-step force-balance computation is available in Appendix A.3.

3.4 | Only missing but at least three (OM3)

Bogner¹⁹ and Thies²⁰ have argued that it is not sufficient to only reconstruct missing PDFs, but it has to be ensured that at least three PDFs are reconstructed (OM3) with the free-surface boundary condition (18). Otherwise, the macroscopic boundary condition at the free interface (17) would be underdetermined. However, neither of these references provides a rigorous mathematical proof for this statement. The authors suggest using the variant from Körner et al.¹ as a fallback in case less than three PDFs are missing in a cell. In this study, this fourth variant will also be investigated numerically using the NBKC variant as fallback for such cases. Formally, the sets K and R are then defined as

$$\begin{aligned} K &:= \begin{cases} \{i | \mathbf{x} - \mathbf{c}_i \Delta t \in \text{non-gas}\} & \text{if } |\{i | \mathbf{x} - \mathbf{c}_i \Delta t \in \text{gas}\}| \geq 3 \\ \{i | \mathbf{n} \cdot \mathbf{c}_i < 0\} & \text{else} \end{cases} \\ R &:= \begin{cases} \{i | \mathbf{x} - \mathbf{c}_i \Delta t \in \text{gas}\} & \text{if } |\{i | \mathbf{x} - \mathbf{c}_i \Delta t \in \text{gas}\}| \geq 3 \\ \{i | \mathbf{n} \cdot \mathbf{c}_i \geq 0\} & \text{else.} \end{cases} \end{aligned} \quad (35)$$

Depending on the number of missing PDFs in the individual interface cell, the resulting force balance will be either similar to the NBKC variant with Equation (29) or OM variant in Equation (34). Consequently, no general error estimate can be made here.

4 | NUMERICAL EXPERIMENTS

This section compares the boundary condition variants introduced and analyzed in Section 3 using five numerical experiments. The chosen test cases are partly identical to the ones suggested in prior articles^{17,22}. They include the simulation of a standing gravity wave, the collapse of a rectangular and cylindrical liquid column, the rise of a Taylor bubble, and the impact of a drop into a thin film of liquid. The description of the test cases, simulation setups, and figures are similar to those from References^{17,22} but are repeated here for completeness. All simulations were performed with double-precision floating-point arithmetic.

4.1 | Gravity wave

A gravity wave is a standing wave with a phase boundary between two immiscible fluids. The wave's flow dynamics are entirely governed by gravitational forces, whereas surface tension forces are neglected. The simulation results were compared to the analytical model^{44,45}.

4.1.1 | Simulation setup

As illustrated in Figure 2, a gravity wave of wavelength L was simulated in a two-dimensional quadratic domain of size $L \times L \times 1$ (x -, y -, z -direction) with $L \in \{200, 400, 800\}$ lattice cells. The interface at the phase boundary was initialized with the profile given by $y(x) = d + a_0 \cos(kx)$ with liquid depth $d = 0.5L$, initial amplitude $a_0 = 0.01L$, and wavenumber $k = 2\pi/L$. In the y -direction, the domain was confined by walls with no-slip boundary conditions, whereas it was periodic in the x -direction. The liquid was initialized with hydrostatic pressure according to the gravitational acceleration g , so the LBM pressure at $y = d$ was equal to the constant atmospheric volume pressure $p^V(t) = p_0$. The relaxation rate $\omega = 1.8$ was chosen and kept constant for any computational domain resolution to conform with diffusive scaling²³. The system is characterized by the Reynolds number

$$\text{Re} := \frac{a_0 \omega_0 L}{\nu} = 10, \quad (36)$$

which is defined with the angular frequency of the wave

$$\omega_0 = \sqrt{gk \tanh(kd)}, \quad (37)$$

and kinematic fluid viscosity ν . Because of the gravitational acceleration g , the initial profile evolved into a standing wave that oscillated around d . It was dampened by viscous forces. The non-dimensionalized surface elevation $a^*(x, t) = a(x, t)/a_0$ and non-dimensionalized time $t^* = t\omega_0$ were monitored at the left domain border, that is, at $x = 0$ every $t^* = 0.01$. The simulations were performed until $t^* = 40$, which was found to be sufficient for the wave's motion to be fully decayed.

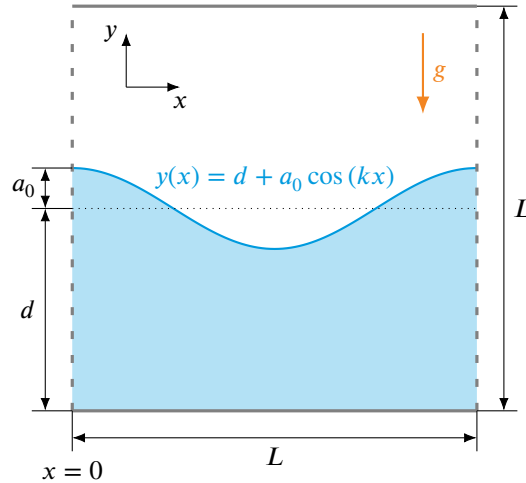


FIGURE 2 Simulation setup of the two-dimensional gravity wave test case with wavelength L , liquid depth d , initial wave amplitude a_0 , wavenumber $k = 2\pi/L$, and gravitational acceleration g . No-slip boundary conditions were used at the domain walls in y -direction. The domain's side walls in the x -direction were periodic. C. Schwarzmeier, M. Holzer, T. Mitchell, M. Lehmann, F. Häusl, U. Rude, Comparison of free surface and conservative Allen–Cahn phase field lattice Boltzmann method, arXiv preprint¹⁷, 2022; licensed under a Creative Commons Attribution (CC BY) license; the colors were changed from the original.

4.1.2 | Analytical model

An analytical model for the gravity wave's motion is derived by linearizing the continuity and Euler equations with a free-surface boundary condition⁴⁴. The standing wave's amplitude

$$a(x, t) = a_D(t) \cos(kx - \omega_0 t) + d, \quad (38)$$

is obtained under the assumption of an inviscid fluid with zero damping $a_D(t) = a_0$. Viscous damping is considered by⁴⁵

$$a_D(t) = a_0 e^{-2\nu k^2 t}. \quad (39)$$

The analytical model is applicable if $k|a_0| \ll 1$ and $k|a_0| \ll kd$ ⁴⁴, which is true in this study with $k|a_0| = 0.02\pi \ll 1 < kd = \pi$.

4.1.3 | Results and discussion

Figure 3 shows the gravity wave simulated with the boundary condition variants presented in Section 3 at a wavelength of $L = 800$ lattice cells. The simulation results with all variants agreed well with the analytical model before $t^* \approx 24$. More noticeable differences are visible in the later course of the simulation. However, it must be pointed out that the FSLBM requires the wave's amplitude to range over at least one, but preferably multiple interface cells to capture the interface's motion significantly well¹⁷. This deficiency of the FSLBM is also visible in the grid convergence study provided in Figure B1 in Appendix B.1. There, it is apparent that the number of meaningfully simulated wave periods decreased when decreasing the computational domain resolution, that is, L . Therefore, the assessment in this test case should be made on the first periods of the simulated wave, where all variants are of similar accuracy.

In summary, the gravity wave test case does not allow a clear conclusion regarding the boundary condition variant to be selected.

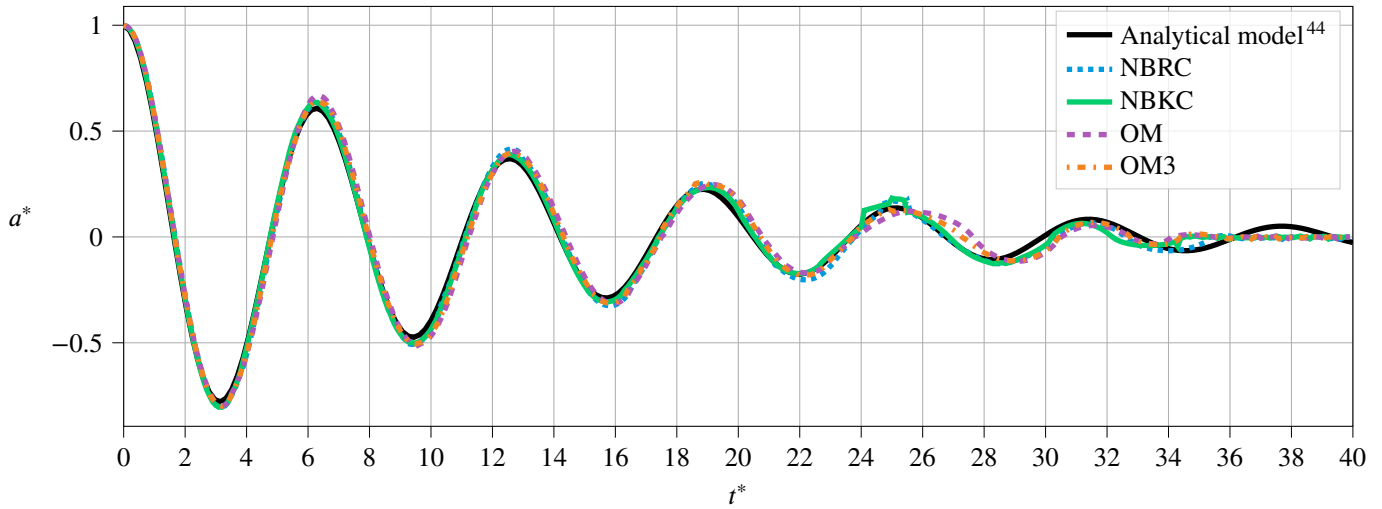


FIGURE 3 Simulated surface elevation of the gravity wave in terms of non-dimensional amplitude $a^*(0, t^*)$ and time t^* . The simulations were performed with a computational domain resolution, that is, wavelength of $L = 800$ lattice cells. The different boundary condition variants show only minor differences and agree well with the analytical model⁴⁴.

4.2 | Rectangular dam break

In a rectangular dam break test case, a rectangular liquid column collapses and spreads at the bottom surface. The test case is regularly used as a numerical benchmark to validate free-surface flow simulations^{6,46,47}. The experiments from Martin and Moyce⁴⁸ were used as reference data for the simulations in this section.

4.2.1 | Simulation setup

The setup was chosen to resemble the reference experiments⁴⁸ and is shown in Figure 4. In a two-dimensional domain of size $15W \times 2H \times 1$ (x -, y -, z -direction), a rectangular liquid column of width $W \in \{50, 100, 200\}$ lattice cells and height $H = 2W$ was positioned at the domain's left wall in the x -direction. The gravitational acceleration g acted in the negative y -direction. Accordingly, the liquid was initialized with hydrostatic pressure, so the LBM pressure at $y = H$ was equal to the constant atmospheric gas pressure $p^V(t) = p_0$. Free-slip boundary conditions were set at all domain borders, and wetting effects were not considered. The chosen relaxation rate $\omega = 1.9995$ was kept constant for all computational domain resolutions as specified by W , conforming with diffusive scaling. The simulations were performed using the turbulence model presented in Section 2.1 with Smagorinsky constant $C_S = 0.1$ ²⁷. The Galilei number

$$\text{Ga} := \frac{gW^3}{\nu^2} = 1.83 \cdot 10^9 \quad (40)$$

relates the gravitational to viscous forces. The Bond number

$$\text{Bo} := \frac{\Delta\rho g W^2}{\sigma} = 445 \quad (41)$$

defines the relation between gravitational and surface tension forces. In these dimensionless numbers, ν is the kinematic viscosity, σ is the surface tension, and $\Delta\rho$ is the density difference between the liquid and the gas phase. Note that $\Delta\rho = \rho$ in a free-surface system, as the gas phase density is assumed to be zero. While the reference experiments⁴⁸ were performed with water, the authors did not provide fluid properties. With given initial column width $W = 0.05715$ m, Ga and Bo as specified above were computed assuming water⁴⁹ at 25 °C with the fluid density $\rho \approx 1000$ kg/m³, kinematic viscosity $\nu \approx 10^{-6}$ m/s², surface tension $\sigma \approx 7.2 \cdot 10^{-2}$ kg/s², and gravitational acceleration $g = 9.81$ m/s².

The liquid column's residual height $h(t)$ and width $w(t)$ were monitored during the simulation, where $h(t)$ was obtained by finding the uppermost interface cell at the left domain wall, that is, at $x = 0$. The width $w(t)$ was obtained by searching for the rightmost interface cell at the bottom domain wall, that is, at $y = 0$. Following Martin and Moyce⁴⁸, the height $h^*(t) := h(t)/H$, width $w^*(t) := w(t)/W$, and time $t^* := t\sqrt{2g/W}$ were non-dimensionalized, with $h^*(t)$ and $w^*(t)$ being monitored every $t^* = 0.01$. In agreement with the experimental data, the simulations were stopped at $w^*(t^*) \geq 14$.

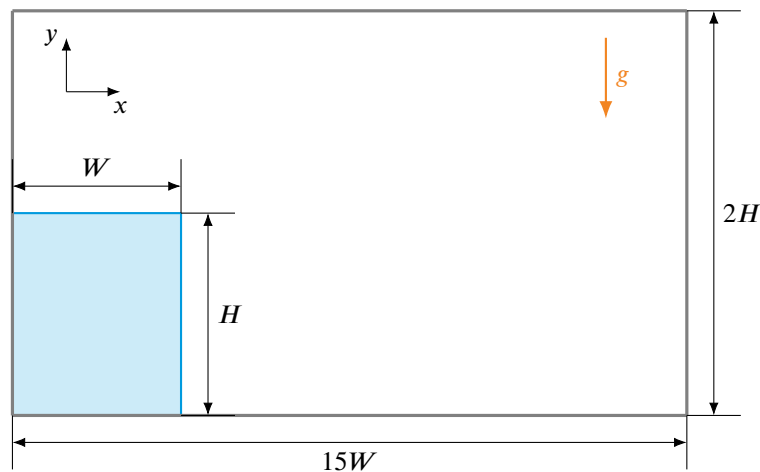


FIGURE 4 Simulation setup of the two-dimensional rectangular dam break test case with the liquid column's initial width W and height H . The gravitational acceleration g acted in negative y -direction and led to the liquid column's collapse. Free-slip boundary conditions were set at all domain walls. C. Schwarzmeier, U. Rude, Comparison of refilling schemes in the free-surface lattice Boltzmann method, arXiv preprint²², 2022; licensed under a Creative Commons Attribution (CC BY) license.

4.2.2 | Results and discussion

Figure 5 shows the spread of the liquid column with an initial width of $W = 200$ lattice cells. All but the NBRC variant produced similarly accurate results and moderately agreed with the experimental data⁴⁸. In contrast, with the NBRC variant, the liquid column's collapse was characterized by the detachment of many droplets, as visualized in Figure 6. Splashing such as this was neither present in the other variants nor reported to be observed in the reference experiments. It was less pronounced at lower computational domain resolutions. However, single droplets were also present in the NBKC and OM3 variants, leading to the sudden jumps in $w^*(t^*)$ in Figure 5. As shown in Figure 7, single droplets separated in the early phase of the dam collapse, moving faster than the liquid front spread. In the case of $W = 100$ with the NBKC variant, the droplet shown in Figure 7 even led to a numerically unstable simulation. There, the droplet's velocity exceeded the lattice speed of sound c_s^2 , which generally is a result of numerical instabilities in the LBM²³.

A grid refinement study of this test case is presented in Figure B2 in Appendix B.2, showing that only the OM variant converged reasonably well. All other variants were subject to the detachment of droplets, as mentioned earlier.

Considering the above observations, the OM variant could be identified as the most accurate for the test case shown here.

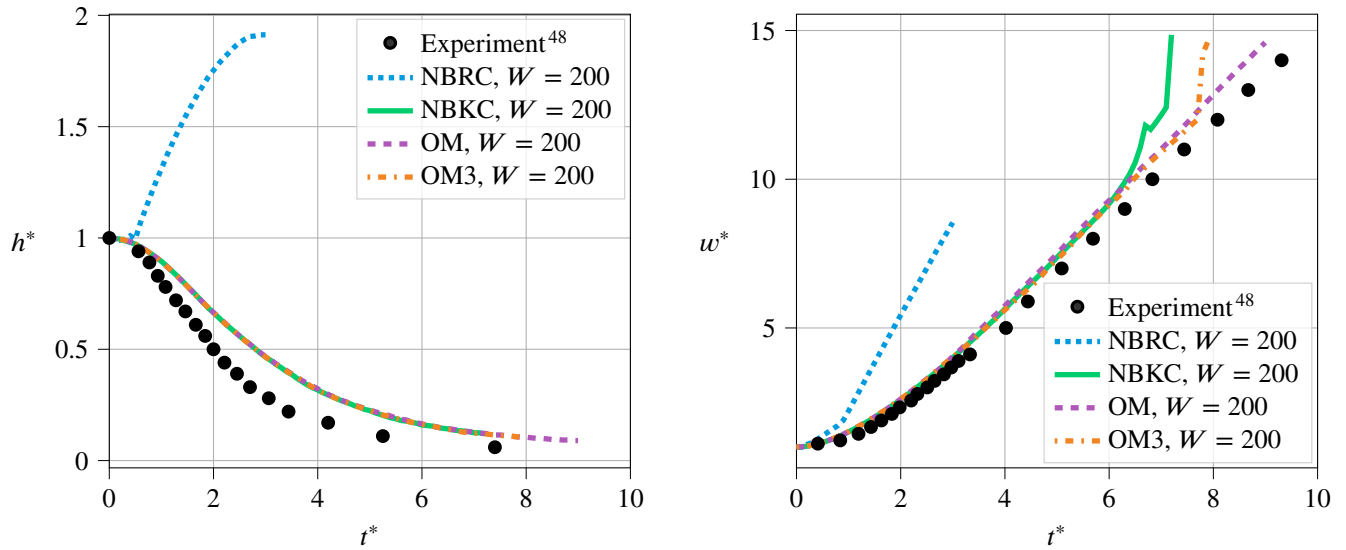


FIGURE 5 Simulated rectangular dam break with non-dimensionalized residual dam height $h^*(t^*)$, width $w^*(t^*)$, and time t^* . The simulations were performed with a computational domain resolution, that is, initial dam width of $W = 200$ lattice cells. The sudden jumps in width observed with the NBKC and OM3 variant were caused by droplets moving faster than the liquid front spread. These droplets separated in the early phase of the dam break, as visualized in Figure 7. Similarly, the droplets shown in Figure 6 for the NBRC variant disturbed the evaluation algorithm and led to the increase of $h^*(t^*)$ rather than to its decrease as expected.

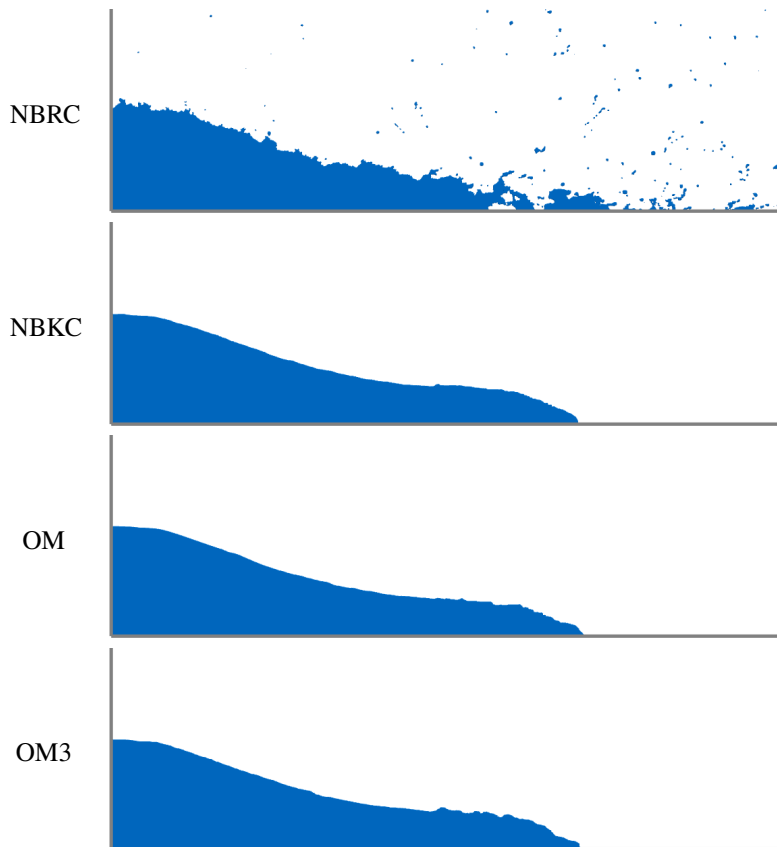


FIGURE 6 Contour of the simulated rectangular dam break at $t^* = 3$ with an initial dam width of $W = 200$ lattice cells. The NBRC variant led to non-physical effects, as splashing was not reported in the reference experiments⁴⁸.



FIGURE 7 Contour of the simulated rectangular dam break at $t^* = 4$ with the NBKC variant and an initial column width of $W = 100$ lattice cells. The droplet marked by the orange circle has detached from the liquid column.

4.3 | Cylindrical dam break

The rectangular dam break test case in Section 4.2 is extended to a cylindrical dam break. The reference experiments are again taken from Martin and Moyce⁴⁸. This test case was chosen to evaluate the effect of the boundary condition variant on the rotational symmetry, as Bogner¹⁸ reported anisotropic artifacts when using a normal-based variant such as the NBKC or NBRC variant.

4.3.1 | Simulation setup

As visualized in Figure 8, a cylindrical liquid column of diameter $D \in \{50, 100, 200\}$ lattice cells and height $H = D$ was placed at the center of the three-dimensional domain of size $6D \times 6D \times 2H$ (x -, y -, z -direction). In other aspects, the setup was similar to the one of the rectangular dam break in Section 4.2.1. However, in the definitions of the Galilei (40) and Bond number (41), the characteristic length $0.5D$ was used.

During the simulation, the liquid column's radius $r(t)$ was monitored. It is defined as the distance of the liquid front to the column's initial center of symmetry such that $r(0) = D/2$. As the liquid column's collapse was observed not to be symmetric in the numerical experiments, $r(t)$ was computed for every interface cell detected by a *seed-fill* algorithm⁵⁰ starting at an arbitrary domain boundary. In practice, this implied that only the outermost interface cells were detected, that is, the interface cells at the spreading liquid's front. A statistical sample was then used to evaluate $r(t)$ by computing the maximum, minimum, and mean values of $r(t)$ at every $t^* = 0.01$. The radius $r^*(t) := 2r(t)/D$ and time $t^* := t\sqrt{4g/D}$ were non-dimensionalized as in the reference data from the literature⁴⁸. In agreement with the reference experiments, the simulations were performed until $r_{\max}^*(t^*) \geq 4.33$, where $r_{\max}^*(t^*)$ is the non-dimensionalized maximum liquid front radius.

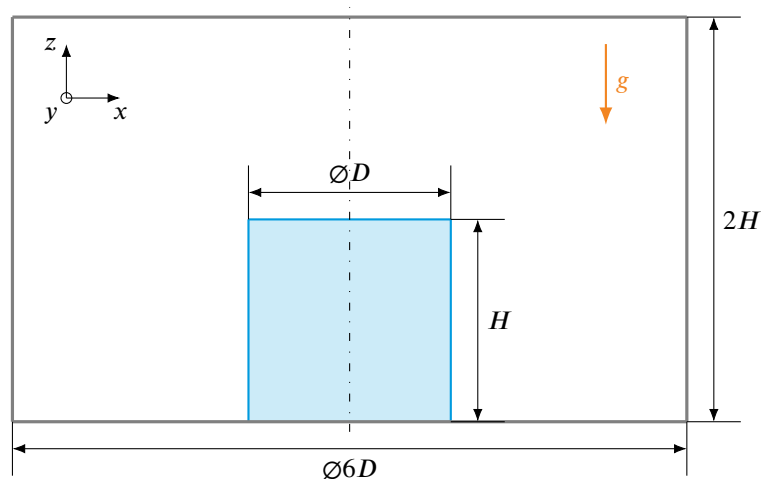


FIGURE 8 Simulation setup of the three-dimensional cylindrical dam break test case. A cylindrical liquid column of diameter D and height H was initialized in the domain's center. It collapsed due to the gravitational acceleration g acting in negative z -direction. Free-slip boundary conditions were set at all domain borders. C. Schwarzmeier, U. Rude, Comparison of refilling schemes in the free-surface lattice Boltzmann method, arXiv preprint²², 2022; licensed under a Creative Commons Attribution (CC BY) license.

4.3.2 | Results and discussion

Figure 9 compares the simulation results for a computational domain resolution equivalent to $D = 200$ lattice cells with the experimental data⁴⁸. The markers show the mean value of the non-dimensionalized radius $r^*(t^*)$. The error bars indicate the maximum and minimum values of $r^*(t^*)$. It is immediately apparent that the OM variant agreed best with the measurements from the literature. It has the smallest error bars in Figure 9, and therefore the lowest standard deviation in $r^*(t^*)$ when compared to the other boundary condition variants. All other variants have significantly larger error bars, indicating that they did not maintain the rotational symmetric nature of the liquid column during its collapse. This observation agrees with the one reported by Bogner¹⁸. Qualitatively, the rotational symmetry during the collapse is shown in Figure 10 at $t^* = 3$. The solid black line indicates the liquid column's initial center of origin. It can be seen that the NBRC and NBKC variants significantly deviated from rotational symmetry.

The grid refinement study is presented in Figure B3 in Appendix B.3 and shows that all of the presented boundary condition variants converged well.

As in the rectangular dam break test case, OM variant was most accurate in this benchmark.

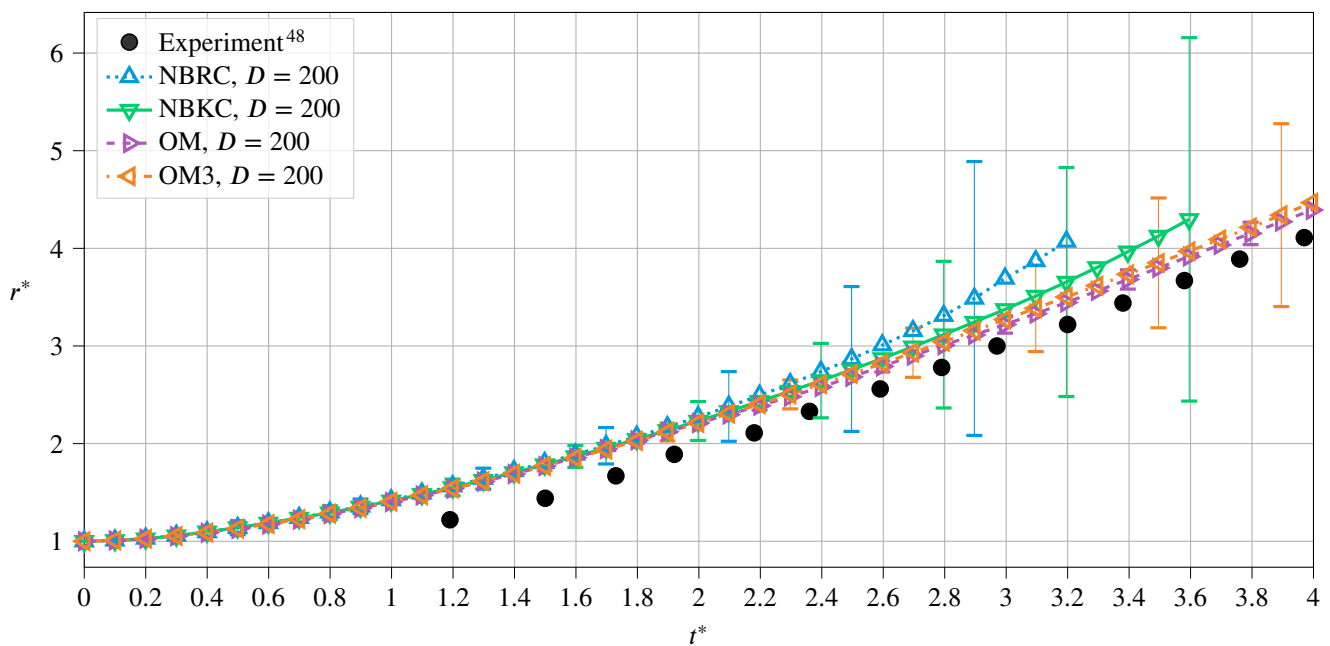


FIGURE 9 Simulated cylindrical dam break with non-dimensionalized liquid column radius $r^*(t^*)$ and time t^* . The simulations were performed with a computational domain resolution, that is, initial column diameter of $D = 200$ lattice cells. The markers represent the mean value of $r^*(t^*)$, and the error bars indicate its maximum and minimum. The OM variant agreed best with the experimental data⁴⁸ and had the smallest error bars. It maintained the column's rotational symmetry better than the other boundary condition variants.

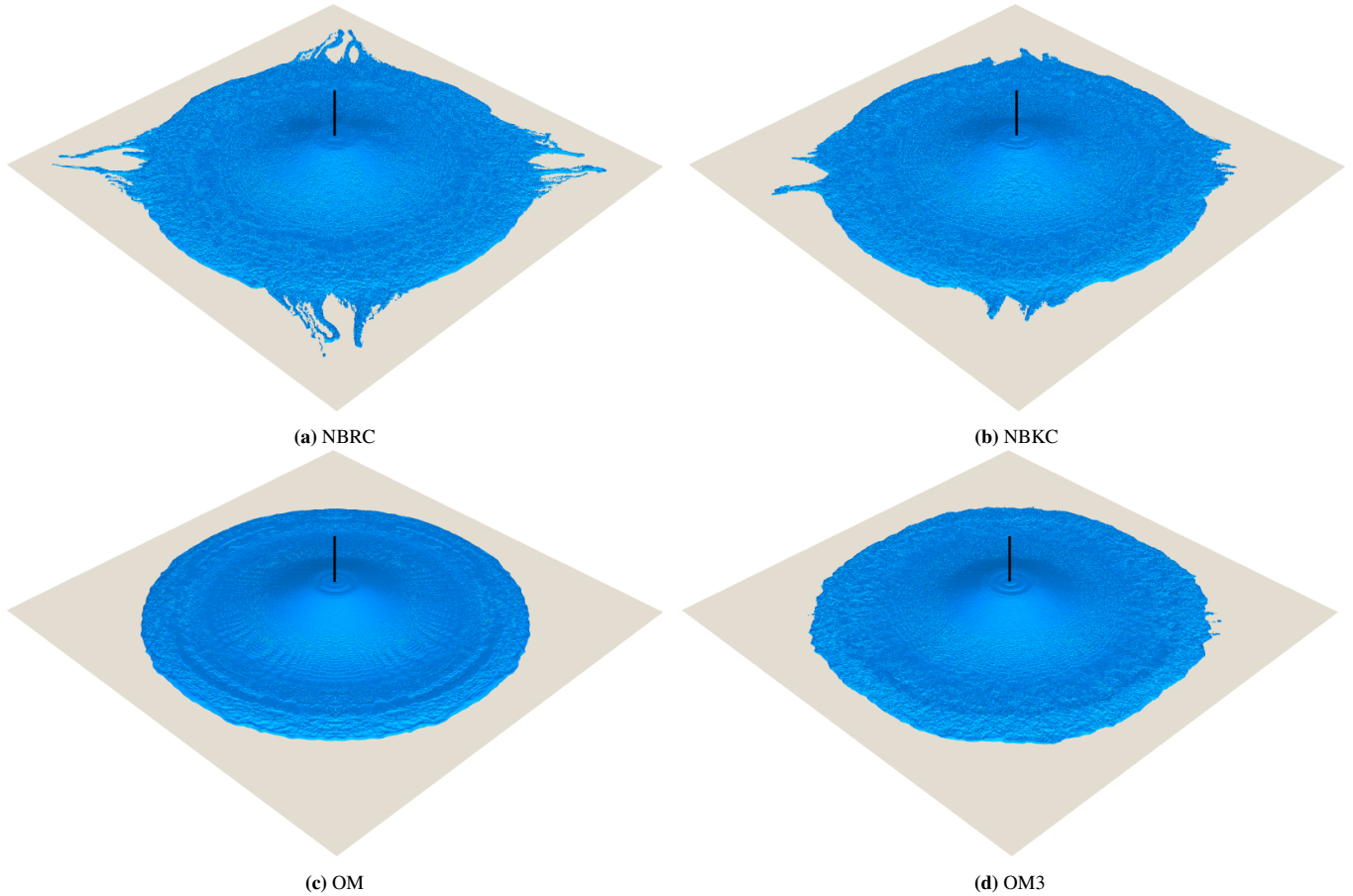


FIGURE 10 Shape of the simulated cylindrical dam break at non-dimensionalized time $t^* = 3$. The simulations were performed with an initial column diameter of $D = 200$ lattice cells. The black line indicates the column's initial center of symmetry. The OM variant maintained the rotational symmetry well, whereas the other approaches showed more deviations.

4.4 | Taylor bubble

A Taylor bubble is a gas bubble rising in a cylindrical tube through stagnant liquid due to buoyancy forces. Its length is multiple times its diameter. It has an elongated shape and its leading edge becomes round. The simulation results were compared to the experimental data from Bugg and Saad⁵¹.

4.4.1 | Simulation setup

The simulation setup resembled that of the reference experiments⁵¹ and is illustrated in Figure 11. The no-slip domain walls formed a cylindrical tube of diameter $D = \{32, 64, 128\}$ lattice cells, pointing in the z -direction in a three-dimensional computational domain of size $1D \times 1D \times 10D$ ($x \times y \times z$). The gas bubble was initialized as a cylinder oriented in the z -direction with a diameter of $0.75D$ and a length of $3D$. It was initially located D above the domain's bottom wall with the volumetric gas pressure $p^V(t) = p_0$. The remainder of the domain was filled with a resting liquid that was initialized with hydrostatic pressure according to the gravitational acceleration g . Therefore, the pressure was initially equivalent to p_0 at $5D$ in the z -direction. All simulations were performed with the relaxation rate $\omega = 1.8$, conforming with diffusive scaling. The fluid mechanics of the setup are characterized by the Morton number

$$\text{Mo} := \frac{g\mu^4}{\rho\sigma^3} = 0.015 \quad (42)$$

that describes the ratio of viscous to surface tension forces. It includes the surface tension σ , the dynamic fluid viscosity μ , and the liquid density ρ . The Bond number $\text{Bo} = 100$ (41), is used with characteristic length D . The evaluations were performed in terms of the non-dimensionalized bubble radius $r^*(t) := r(t)/(0.5D)$, axial location $z^*(t) := z(t)/D$, and time $t^* := t\sqrt{g/D}$.

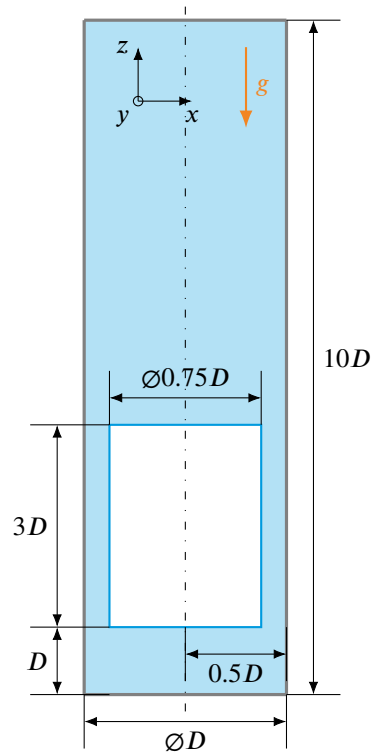


FIGURE 11 Simulation setup of the three-dimensional Taylor bubble test case with an initially cylindrical gas bubble in a cylindrical tube of diameter D . The gravitational acceleration g acted in the negative z -direction. No-slip boundary conditions were applied at the tube and all domain walls. C. Schwarzmeier, M. Holzer, T. Mitchell, M. Lehmann, F. Häusl, U. Rüde, Comparison of free surface and conservative Allen-Cahn phase field lattice Boltzmann method, arXiv preprint¹⁷, 2022; licensed under a Creative Commons Attribution (CC BY) license; the colors were changed from the original.

4.4.2 | Results and discussion

The simulated Reynolds number

$$\text{Re} := \frac{Du}{\nu} \quad (43)$$

is listed in Table 1 for different tube diameters D . Re is computed with the kinematic viscosity ν and the bubble's rise velocity u . The latter was obtained from the bubble's center of mass in the z -direction at times $t^* = 10$ and $t^* = 15$. All boundary condition variants agreed reasonably well with the experimental data. The OM variant was the most accurate with an error of approximately 4% at $D = 128$. Figure 12 compares the bubble's shape at its front and tail at time $t^* = 15$ with the experimental observations. All variants generally produced plausible results. The OM variant most closely resembled the bubble's shape from the experimental measurements. For the other variants, no clear trend is visible.

The grid refinement study in Table 1 and Figure B4 in Appendix B.4 shows that all boundary condition variants converged well. As in both dam break test cases, the OM variant was the most accurate in this benchmark.

D	32	64	128
Re_{NBRC}	21.92	23.77	25.12
Re_{NBKC}	20.98	22.86	24.27
Re_{OM}	24.12	25.35	25.89
Re_{OM3}	22.68	23.96	24.74
$Re_{Experiment}^{51}$		27	

TABLE 1 Reynolds number Re of the simulated Taylor bubble for different computational domain resolutions as specified by the tube diameter D . The bubble's rise velocity, as used to compute Re , was obtained from the Taylor bubble's location in axial direction at time $t^* = 10$ and $t^* = 15$.

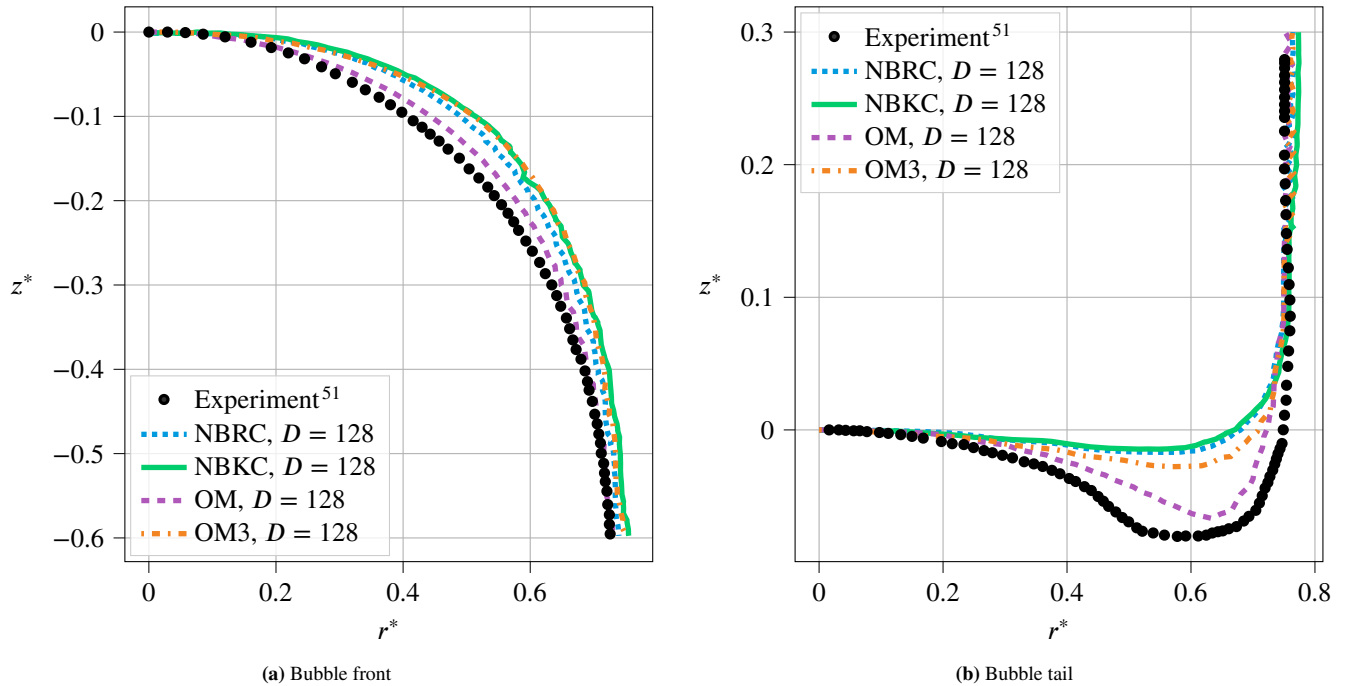


FIGURE 12 Simulated shape of the Taylor bubble's front and tail. The simulations were performed with a computational domain resolution, that is, tube diameter of $D = 128$ lattice cells. The comparison with experimental data⁵¹ was drawn in terms of the non-dimensionalized axial location z^* and radial location r^* at time $t^* = 15$. The OM variant was most accurate.

4.5 | Drop impact

In the final test case, the vertical impact of a drop into a pool of liquid was simulated. Due to the lack of quantitative experimental data in the reference experiments from Wang and Chen⁵², only a qualitative comparison with a photograph could be made here.

4.5.1 | Simulation setup

The simulation setup was chosen to conform with the reference experiments⁵². As illustrated in Figure 13, a spherical droplet with a diameter of $D = 80$ lattice cells was initialized in a three-dimensional computational domain of size $10D \times 10D \times 5D$ (x -, y -, z -direction) lattice cells. The droplet was located at the surface of a thin liquid film of height $0.5D$ and had an initialized impact velocity U in the negative z -direction. The gravitational acceleration g also acted in the negative z -direction. In the drop and in the liquid film, hydrostatic pressure according to g was initialized. Accordingly, the pressure at the pool's surface was equal to the constant atmospheric volumetric gas pressure $p^V(t) = p_0$. There were no-slip boundary conditions at the top and bottom domain walls in the z -direction. The domain walls in the x - and y -direction were periodic. The relaxation rate was chosen

$\omega = 1.989$. The droplet's impact is described by the Weber number

$$\text{We} := \frac{\rho U^2 D}{\sigma} = 2010 \quad (44)$$

that relates inertial and surface tension forces, and the Ohnesorge number

$$\text{Oh} := \frac{\mu}{\sqrt{\sigma \rho D}} = 0.0384 \quad (45)$$

that relates viscous to inertial and surface tension forces. These dimensionless numbers include the surface tension σ , dynamic viscosity μ , and liquid density ρ .

A fluid with density $\rho = 1200 \text{ kg/m}^3$ and dynamic viscosity $\mu = 0.022 \text{ kg/(m}\cdot\text{s)}$ was used in the experiments⁵². Assuming $g = 9.81 \text{ m/s}^2$, the definition of the system is closed by $\text{Bo} = 3.18$ (41) with characteristic length D . As observed by Lehmann et al.⁷, the non-dimensionalized time $t^* := tU/D$ must be offset by $t^* = 0.16$ for comparison with the numerical simulations as set up in the study here.

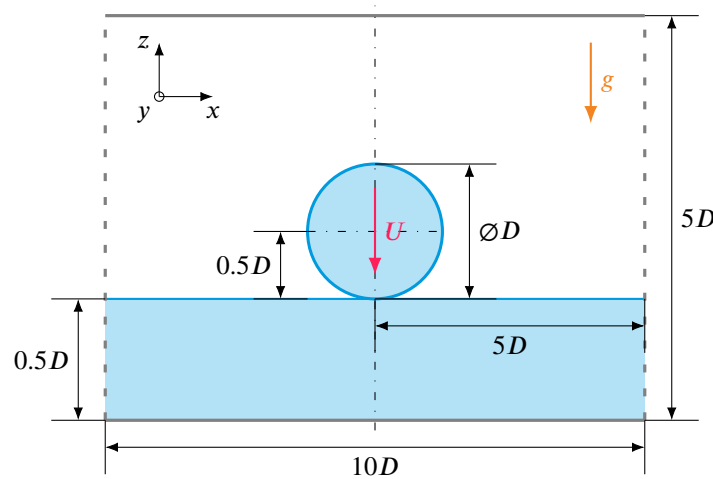


FIGURE 13 Simulation setup of the drop impact test case. A spherical drop of liquid with diameter D was initialized right above the surface of a liquid pool of height $0.5D$ in a domain of size $10D \times 10D \times 5D$. The gravitational acceleration g acted in the negative z -direction and the droplet was initialized with impact velocity U in the same direction. The domain's side walls in x - and y -direction were periodic, whereas the domain's top and bottom walls in z -direction were set to no-slip. C. Schwarzmeier, M. Holzer, T. Mitchell, M. Lehmann, F. Häusl, U. Rüde, Comparison of free surface and conservative Allen–Cahn phase field lattice Boltzmann method, arXiv preprint¹⁷, 2022; licensed under a Creative Commons Attribution (CC BY) license; the colors were changed from the original.

4.5.2 | Results and discussion

Figure 14 shows the drop impact, that is, splash crown formation at $t^* = 12$ with the solid black line indicating the contour in a central cross-section with normal in the x -direction. Since no scale bars are provided in the photographs of the experiment⁵², the simulations could only be validated and compared qualitatively. Visually, the OM variant produced the most realistic results. More specifically, in agreement with the observations for the cylindrical dam break in Section 4.3.2, it showed the least anisotropic behavior of all tested variants. In contrast, the NBRC and NBKC variant overestimated splashing, that is, the detachment of smaller droplets. However, these droplets had the shape of a thread rather than of a sphere as in the reference experiments. Eventually, the droplets fell due to the influence of gravity and reached the liquid film's surface, as can be seen by the impacts there. The OM3 variant was more accurate than the normal-based variants but was also subject to anisotropy, as clearly visible in the side view in Figure 14.

Again, as in the numerical experiments from the preceding sections, the OM variant was the most accurate in this test case.

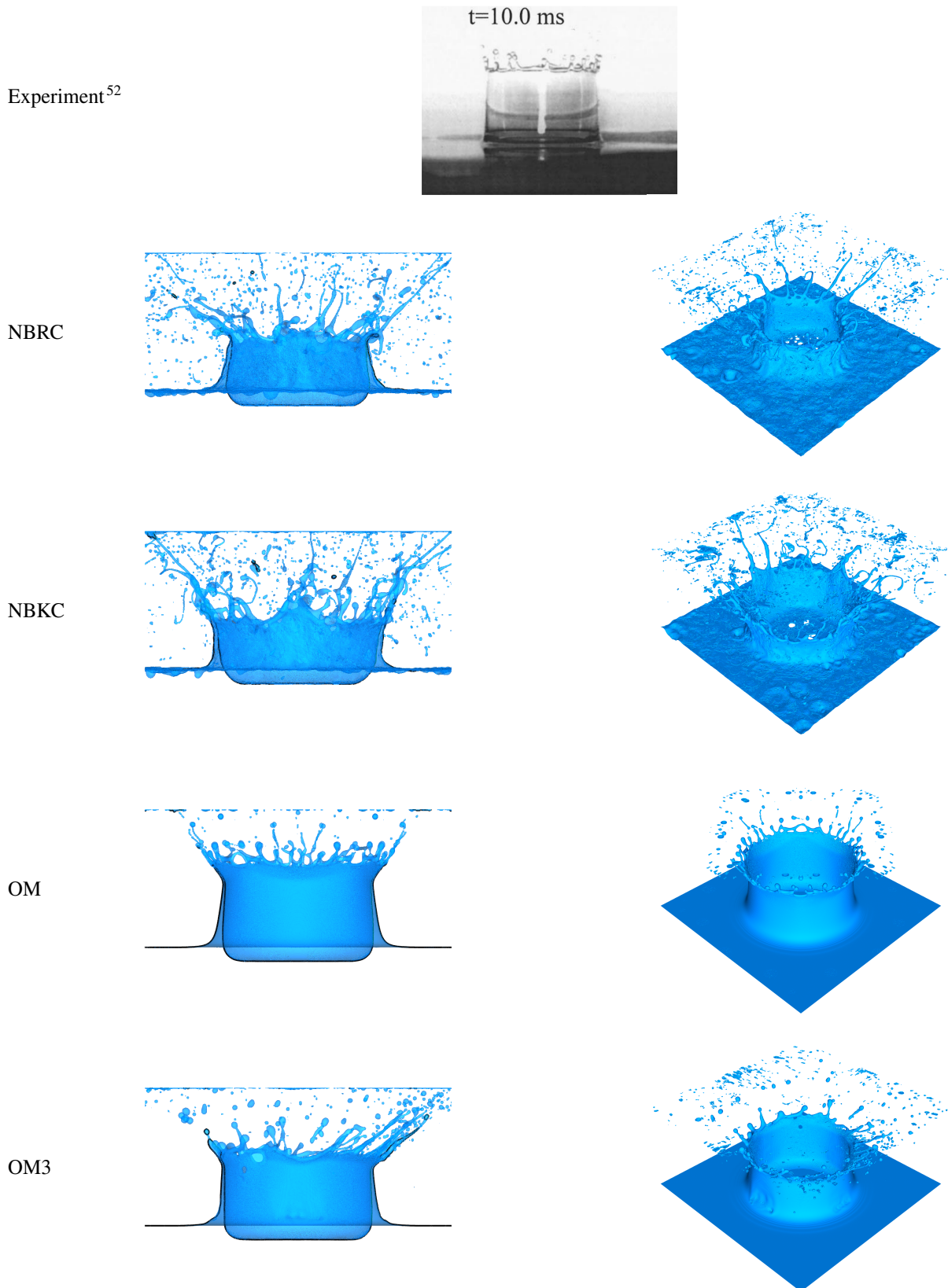


FIGURE 14 Simulated splash crown of the drop impact at non-dimensionalized time $t^* = 12$. The simulations were performed with a computational domain resolution, that is, initial drop diameter of $D = 80$ lattice cells. The solid black lines illustrate the crown's contour in a centrally located cross-section with normal in the x -direction. All but the OM variant showed significant anisotropic artifacts. In the NBRC and NBKC variant, droplets that have detached from the splash crown in an earlier phase, have already hit the liquid pool's surface. The photograph of the laboratory experiment is reproduced from A.-B. Wang, C.-C. Chen, Splashing impact of a single drop onto very thin liquid films⁵², *Physics of Fluids*, 12, 2000, with the permission of AIP Publishing.

5 | CONCLUSIONS

In this study, different variants for free-surface boundary conditions in the FSLBM¹ were compared. The FSLBM assumes a free surface and neglects the fluid dynamics in the gas phase of a liquid–gas system. Accordingly, no PDFs are stored in the gas phase, and PDFs streaming from gas cells to interface cells must be reconstructed with a free-surface boundary condition. In the original formulation of the FSLBM, these missing PDFs are reconstructed based on the orientation of the interface-normal¹. However, with this approach, existing information about the flow field is overwritten. The authors argued that this would be required to balance the forces exerted by the liquid and gas pressure.

In this article, four different variants for reconstructing missing PDFs were under investigation. These include normal-based variants, where the central PDF is reconstructed (NBRC)¹ or kept (NBKC). As opposed to these, only missing PDFs are reconstructed in the OM variant. In the OM3 variant, only missing but at least three PDFs are reconstructed^{19,20}, falling back to the NBKC variant otherwise.

It was mathematically shown that neither of the variants generally balances the forces at a free interface in motion. However, the OM variant was found to be the most accurate in five numerical experiments, whereas the other variants were subject to anisotropic artifacts and numerical instabilities. It can be concluded that for the FSLBM¹ considered in this article, only missing PDFs should be reconstructed, and no information about the flow field should be dropped.

ACKNOWLEDGMENTS

The authors thank the Deutsche Forschungsgemeinschaft (DFG, German Research Foundation) for funding project 408062554. This work was supported by the SCALABLE project. This project has received funding from the European High-Performance Computing Joint Undertaking (JU) under grant agreement No 956000. The JU receives support from the European Union's Horizon 2020 research and innovation programme and France, Germany, the Czech Republic.

The authors gratefully acknowledge the Gauss Centre for Supercomputing e.V. (www.gauss-centre.eu) for funding this project by providing computing time on the GCS Supercomputer SuperMUC at Leibniz Supercomputing Centre (www.lrz.de).

The authors gratefully acknowledge the scientific support and HPC resources provided by the Erlangen National High Performance Computing Center (NHR@FAU) of the Friedrich-Alexander-Universität Erlangen-Nürnberg (FAU). The hardware is funded by the German Research Foundation (DFG).

The authors appreciate the valuable discussions with Christoph Rettinger and Simon Bogner, and thank Sara Faghih-Naini and Jonas Plewinski for proofreading the manuscript.

Financial disclosure

None reported.

Conflict of interest

The authors declare no potential conflict of interests.

SUPPORTING INFORMATION

The following supporting information is available as part of the online article:

An archive of the C++ source code used in this study. It is part of the software framework waLBerla (version used here: <https://i10git.cs.fau.de/walberla/walberla/-/tree/01a28162ae1aacf7b96152c9f886ce54cc7f53ff>). The ready-to-run simulation setups for all numerical experiments performed in this article are included in the directory `apps/showcases/FreeSurface`.

How to cite this article: Schwarzmeier C, Rude U. **Analysis and comparison of boundary condition variants in the free surface lattice Boltzmann method.** *Int J Numer Meth Fluids*. 2022, XXX.

APPENDIX

A FORCE-BALANCE COMPUTATION

This section provides the step-by-step computation of the force balance at the free interface for the boundary condition variants presented in Section 3.

A.1 Normal-based, reconstruct center (NBRC)

Using the definitions of K , R (26) and the free-surface boundary condition (18), the general force balance (24) becomes

$$\begin{aligned}
\frac{F_\alpha}{A} &= -n_\beta \sum_{i \in \{i | \mathbf{n} \cdot \mathbf{c}_i < 0\}} f_i^*(\mathbf{x}, t)(c_{i,\alpha} - u_\alpha)(c_{i,\beta} - u_\beta) \\
&\quad - n_\beta \sum_{i \in \{i | \mathbf{n} \cdot \mathbf{c}_i \geq 0\}} \left(f_i^{\text{eq}}(\rho^G, \mathbf{u}) + f_{\bar{i}}^{\text{eq}}(\rho^G, \mathbf{u}) - f_{\bar{i}}^*(\mathbf{x}, t) \right) (c_{i,\alpha} - u_\alpha)(c_{i,\beta} - u_\beta) \\
&= -n_\beta \sum_{i \in \{i | \mathbf{n} \cdot \mathbf{c}_i < 0\}} f_i^*(\mathbf{x}, t)(c_{i,\alpha} - u_\alpha)(c_{i,\beta} - u_\beta) + n_\beta \sum_{i \in \{i | \mathbf{n} \cdot \mathbf{c}_i \geq 0\}} f_{\bar{i}}^*(\mathbf{x}, t)(c_{i,\alpha} - u_\alpha)(c_{i,\beta} - u_\beta) \\
&\quad - n_\beta \sum_{i \in \{i | \mathbf{n} \cdot \mathbf{c}_i \geq 0\}} f_i^{\text{eq}}(\rho^G, \mathbf{u})(c_{i,\alpha} - u_\alpha)(c_{i,\beta} - u_\beta) - n_\beta \sum_{i \in \{i | \mathbf{n} \cdot \mathbf{c}_i \geq 0\}} f_{\bar{i}}^{\text{eq}}(\rho^G, \mathbf{u})(c_{i,\alpha} - u_\alpha)(c_{i,\beta} - u_\beta).
\end{aligned} \tag{A1}$$

Each PDF in a cell can either be left unmodified or reconstructed but not both at the same time. Consequently, a PDF can only be exclusively in either $\{i | \mathbf{n} \cdot \mathbf{c}_i < 0\}$ or $\{i | \mathbf{n} \cdot \mathbf{c}_i \geq 0\}$. The union of these sets must contain all q PDFs of the cell. These conditions are formally denoted as

$$\{i | \mathbf{n} \cdot \mathbf{c}_i \geq 0\} \cap \{i | \mathbf{n} \cdot \mathbf{c}_i < 0\} \stackrel{!}{=} \emptyset \quad \wedge \quad \{i | \mathbf{n} \cdot \mathbf{c}_i \geq 0\} \cup \{i | \mathbf{n} \cdot \mathbf{c}_i < 0\} \stackrel{!}{=} \{0, 1, \dots, q-1\} \tag{A2}$$

where q is defined by the chosen velocity set $DdQq$. In the velocity sets generally employed for simulating hydrodynamics with the LBM, the central lattice velocity is zero, $\mathbf{c}_0 = \mathbf{0}^{23}$. Accordingly, the corresponding dot product with the interface-normal \mathbf{n} is also zero, $\mathbf{n} \cdot \mathbf{c}_0 = 0$. This implies that with $K = \{i | \mathbf{n} \cdot \mathbf{c}_i < 0\}$ and $R = \{i | \mathbf{n} \cdot \mathbf{c}_i \geq 0\}$ chosen as by Körner et al.¹, the central post-collision PDF f_0^* must be reconstructed. Without loss of generality, it is assumed now that the normal is non-zero $\mathbf{n} \neq \mathbf{0}$ to simplify the analysis. Then, $\mathbf{n} \cdot \mathbf{c}_i = 0$ if and only if $i = 0 = \bar{i}$.

The central PDF f_0 is extracted from the second sum in the force balance (A1)

$$\begin{aligned}
&\sum_{i \in \{i | \mathbf{n} \cdot \mathbf{c}_i \geq 0\}} f_{\bar{i}}^*(\mathbf{x}, t)(c_{i,\alpha} - u_\alpha)(c_{i,\beta} - u_\beta) \\
&= f_0^*(\mathbf{x}, t)u_\alpha u_\beta + \sum_{i \in \{i | \mathbf{n} \cdot \mathbf{c}_i > 0\}} f_{\bar{i}}^*(\mathbf{x}, t)(c_{i,\alpha} - u_\alpha)(c_{i,\beta} - u_\beta) \\
&= f_0^*(\mathbf{x}, t)u_\alpha u_\beta + \sum_{i \in \{i | -\mathbf{n} \cdot \mathbf{c}_{\bar{i}} > 0\}} f_{\bar{i}}^*(\mathbf{x}, t)(-c_{\bar{i},\alpha} - u_\alpha)(-c_{\bar{i},\beta} - u_\beta) \\
&= f_0^*(\mathbf{x}, t)u_\alpha u_\beta + \sum_{i \in \{i | \mathbf{n} \cdot \mathbf{c}_{\bar{i}} < 0\}} f_{\bar{i}}^*(\mathbf{x}, t)(c_{\bar{i},\alpha} + u_\alpha)(c_{\bar{i},\beta} + u_\beta) \\
&= f_0^*(\mathbf{x}, t)u_\alpha u_\beta + \sum_{i \in \{i | \mathbf{n} \cdot \mathbf{c}_i < 0\}} f_i^*(\mathbf{x}, t)(c_{i,\alpha} + u_\alpha)(c_{i,\beta} + u_\beta),
\end{aligned} \tag{A3}$$

where the range of the sum $i \in \{i | \mathbf{n} \cdot \mathbf{c}_i > 0\}$ was reverted to $i \in \{i | \mathbf{n} \cdot \mathbf{c}_i < 0\}$, with $f_{\bar{i}}$ referring to the PDF for the direction $\mathbf{c}_{\bar{i}} = -\mathbf{c}_i$. In the last step, \bar{i} was substituted with i . It is important to note that the substitution changes the effective indices of the sum, as the corresponding set defining the indices is also changed. Analogously, f_0^{eq} is extracted from the fourth sum in the force balance (A1) giving

$$\begin{aligned}
&\sum_{i \in \{i | \mathbf{n} \cdot \mathbf{c}_i \geq 0\}} f_{\bar{i}}^{\text{eq}}(\rho^G, \mathbf{u})(c_{i,\alpha} - u_\alpha)(c_{i,\beta} - u_\beta) \\
&= f_0^{\text{eq}}(\rho^G, \mathbf{u})u_\alpha u_\beta + \sum_{i \in \{i | \mathbf{n} \cdot \mathbf{c}_i < 0\}} f_i^{\text{eq}}(\rho^G, \mathbf{u})(c_{i,\alpha} + u_\alpha)(c_{i,\beta} + u_\beta).
\end{aligned} \tag{A4}$$

Inserting the transformations (A3) and (A4) in the force balance (A1) gives

$$\begin{aligned}
\frac{F_\alpha}{A} &= -n_\beta \sum_{i \in \{i | n \cdot c_i < 0\}} f_i^*(\mathbf{x}, t)(c_{i,\alpha} - u_\alpha)(c_{i,\beta} - u_\beta) \\
&\quad + n_\beta \left(f_0^*(\mathbf{x}, t)u_\alpha u_\beta + \sum_{i \in \{i | n \cdot c_i < 0\}} f_i^*(\mathbf{x}, t)(c_{i,\alpha} + u_\alpha)(c_{i,\beta} + u_\beta) \right) \\
&\quad - n_\beta \sum_{i \in \{i | n \cdot c_i \geq 0\}} f_i^{\text{eq}}(\rho^G, \mathbf{u})(c_{i,\alpha} - u_\alpha)(c_{i,\beta} - u_\beta) \\
&\quad - n_\beta \left(f_0^{\text{eq}}(\rho^G, \mathbf{u})u_\alpha u_\beta + \sum_{i \in \{i | n \cdot c_i < 0\}} f_i^{\text{eq}}(\rho^G, \mathbf{u})(c_{i,\alpha} + u_\alpha)(c_{i,\beta} + u_\beta) \right) \\
&= -n_\beta \sum_{i \in \{i | n \cdot c_i < 0\}} f_i^*(\mathbf{x}, t)(c_{i,\alpha}c_{i,\beta} - c_{i,\alpha}u_\beta - c_{i,\beta}u_\alpha + u_\alpha u_\beta) \\
&\quad + n_\beta f_0^*(\mathbf{x}, t)u_\alpha u_\beta + n_\beta \sum_{i \in \{i | n \cdot c_i < 0\}} f_i^*(\mathbf{x}, t)(c_{i,\alpha}c_{i,\beta} + c_{i,\alpha}u_\beta + c_{i,\beta}u_\alpha + u_\alpha u_\beta) \\
&\quad - n_\beta \sum_{i \in \{i | n \cdot c_i \geq 0\}} f_i^{\text{eq}}(\rho^G, \mathbf{u})(c_{i,\alpha}c_{i,\beta} - c_{i,\alpha}u_\beta - c_{i,\beta}u_\alpha + u_\alpha u_\beta) \\
&\quad - n_\beta f_0^{\text{eq}}(\rho^G, \mathbf{u})u_\alpha u_\beta - n_\beta \sum_{i \in \{i | n \cdot c_i < 0\}} f_i^{\text{eq}}(\rho^G, \mathbf{u})(c_{i,\alpha}c_{i,\beta} + c_{i,\alpha}u_\beta + c_{i,\beta}u_\alpha + u_\alpha u_\beta) \\
&= n_\beta \left(f_0^*(\mathbf{x}, t) - f_0^{\text{eq}}(\rho^G, \mathbf{u}) \right) u_\alpha u_\beta \\
&\quad + 2n_\beta \sum_{i \in \{i | n \cdot c_i < 0\}} f_i^*(\mathbf{x}, t)(c_{i,\alpha}u_\beta + c_{i,\beta}u_\alpha) \\
&\quad - n_\beta \sum_i f_i^{\text{eq}}(\rho^G, \mathbf{u})(c_{i,\alpha}c_{i,\beta} + u_\alpha u_\beta) \\
&\quad + n_\beta \sum_{i \in \{i | n \cdot c_i \geq 0\}} f_i^{\text{eq}}(\rho^G, \mathbf{u})(c_{i,\alpha}u_\beta + c_{i,\beta}u_\alpha) - n_\beta \sum_{i \in \{i | n \cdot c_i < 0\}} f_i^{\text{eq}}(\rho^G, \mathbf{u})(c_{i,\alpha}u_\beta + c_{i,\beta}u_\alpha),
\end{aligned} \tag{A5}$$

where in the last step, the sets' property (A2) was used to combine the summands containing $f_i^{\text{eq}}(\rho^G, \mathbf{u})$ from different sums. The final two sums of the force balance (A5) are extended with zero by adding and subtracting $n_\beta \sum_{i \in \{i | n \cdot c_i < 0\}} f_i^{\text{eq}}(\rho^G, \mathbf{u})(c_{i,\alpha}u_\beta + c_{i,\beta}u_\alpha)$, which leads to

$$\begin{aligned}
&n_\beta \sum_{i \in \{i | n \cdot c_i \geq 0\}} f_i^{\text{eq}}(\rho^G, \mathbf{u})(c_{i,\alpha}u_\beta + c_{i,\beta}u_\alpha) - n_\beta \sum_{i \in \{i | n \cdot c_i < 0\}} f_i^{\text{eq}}(\rho^G, \mathbf{u})(c_{i,\alpha}u_\beta + c_{i,\beta}u_\alpha) \\
&= n_\beta \sum_{i \in \{i | n \cdot c_i \geq 0\}} f_i^{\text{eq}}(\rho^G, \mathbf{u})(c_{i,\alpha}u_\beta + c_{i,\beta}u_\alpha) + n_\beta \sum_{i \in \{i | n \cdot c_i < 0\}} f_i^{\text{eq}}(\rho^G, \mathbf{u})(c_{i,\alpha}u_\beta + c_{i,\beta}u_\alpha) \\
&\quad - n_\beta \sum_{i \in \{i | n \cdot c_i < 0\}} f_i^{\text{eq}}(\rho^G, \mathbf{u})(c_{i,\alpha}u_\beta + c_{i,\beta}u_\alpha) - n_\beta \sum_{i \in \{i | n \cdot c_i < 0\}} f_i^{\text{eq}}(\rho^G, \mathbf{u})(c_{i,\alpha}u_\beta + c_{i,\beta}u_\alpha) \\
&= n_\beta \sum_i f_i^{\text{eq}}(\rho^G, \mathbf{u})(c_{i,\alpha}u_\beta + c_{i,\beta}u_\alpha) - 2n_\beta \sum_{i \in \{i | n \cdot c_i < 0\}} f_i^{\text{eq}}(\rho^G, \mathbf{u})(c_{i,\alpha}u_\beta + c_{i,\beta}u_\alpha),
\end{aligned} \tag{A6}$$

where again the sets' property (A2) was used to combine the sums ranging over different sets.

The final expression for the balance of the forces is obtained when inserting the transformation (A6) into the force balance (A5)

$$\begin{aligned}
\frac{F_\alpha}{A} &= n_\beta \left(f_0^*(\mathbf{x}, t) - f_0^{\text{eq}}(\rho^G, \mathbf{u}) \right) u_\alpha u_\beta \\
&\quad + 2n_\beta \sum_{i \in \{i | \mathbf{n} \cdot \mathbf{c}_i < 0\}} f_i^*(\mathbf{x}, t) (c_{i,\alpha} u_\beta + c_{i,\beta} u_\alpha) \\
&\quad - n_\beta \sum_i f_i^{\text{eq}}(\rho^G, \mathbf{u}) (c_{i,\alpha} c_{i,\beta} + u_\alpha u_\beta - c_{i,\alpha} u_\beta - c_{i,\beta} u_\alpha) \\
&\quad - 2n_\beta \sum_{i \in \{i | \mathbf{n} \cdot \mathbf{c}_i < 0\}} f_i^{\text{eq}}(\rho^G, \mathbf{u}) (c_{i,\alpha} u_\beta + c_{i,\beta} u_\alpha) \\
&= n_\beta \left(f_0^*(\mathbf{x}, t) - f_0^{\text{eq}}(\rho^G, \mathbf{u}) \right) u_\alpha u_\beta \\
&\quad + 2n_\beta \left(\sum_{i \in \{i | \mathbf{n} \cdot \mathbf{c}_i < 0\}} f_i^*(\mathbf{x}, t) (c_{i,\alpha} u_\beta + c_{i,\beta} u_\alpha) - \sum_{i \in \{i | \mathbf{n} \cdot \mathbf{c}_i < 0\}} f_i^{\text{eq}}(\rho^G, \mathbf{u}) (c_{i,\alpha} u_\beta + c_{i,\beta} u_\alpha) \right) \\
&\quad - n_\beta (\rho^G c_s^2 \delta_{\alpha\beta} + \rho^G u_\alpha u_\beta + \rho^G u_\alpha u_\beta - \rho^G u_\alpha u_\beta - \rho^G u_\alpha u_\beta) \\
&= n_\beta \left(f_0^*(\mathbf{x}, t) - f_0^{\text{eq}}(\rho^G, \mathbf{u}) \right) u_\alpha u_\beta \\
&\quad + 2n_\beta \sum_{i \in \{i | \mathbf{n} \cdot \mathbf{c}_i < 0\}} \left(f_i^*(\mathbf{x}, t) - f_i^{\text{eq}}(\rho^G, \mathbf{u}) \right) (c_{i,\alpha} u_\beta + c_{i,\beta} u_\alpha) \\
&\quad - n_\alpha p^G,
\end{aligned} \tag{A7}$$

where $p^G = \rho c_s^2$ was used. This result has been obtained using the equilibrium moments²³

$$\begin{aligned}
\Pi^{\text{eq}}(\rho^G, \mathbf{u}) &= \sum_i f_i^{\text{eq}}(\rho^G, \mathbf{u}) = \rho^G \\
\Pi_\alpha^{\text{eq}}(\rho^G, \mathbf{u}) &= \sum_i f_i^{\text{eq}}(\rho^G, \mathbf{u}) c_{i,\alpha} = \rho^G u_\alpha \\
\Pi_{\alpha\beta}^{\text{eq}}(\rho^G, \mathbf{u}) &= \sum_i f_i^{\text{eq}}(\rho^G, \mathbf{u}) c_{i,\alpha} c_{i,\beta} = \rho^G c_s^2 \delta_{\alpha\beta} + \rho^G u_\alpha u_\beta,
\end{aligned} \tag{A8}$$

where $\delta_{\alpha\beta}$ is the Kronecker delta. The balance of the forces at the interface is disturbed by the expression

$$n_\beta \left(f_0^*(\mathbf{x}, t) - f_0^{\text{eq}}(\rho^G, \mathbf{u}) \right) u_\alpha u_\beta + 2n_\beta \sum_{i \in \{i | \mathbf{n} \cdot \mathbf{c}_i < 0\}} \left(f_i^*(\mathbf{x}, t) - f_i^{\text{eq}}(\rho^G, \mathbf{u}) \right) (c_{i,\alpha} u_\beta + c_{i,\beta} u_\alpha). \tag{A9}$$

A.2 Normal-based, keep center (NBKC)

Using the same procedure as for the NBRC in Appendix A.1 but replacing $\mathbf{n} \cdot \mathbf{c}_i \geq 0$ with $\mathbf{n} \cdot \mathbf{c}_i > 0$, the additional terms for $i = 0$ vanish in the transformations (A3) and (A4), so that the force balance (A5) becomes

$$\begin{aligned}
\frac{F_\alpha}{A} &= -n_\beta \sum_{i \in \{i | \mathbf{n} \cdot \mathbf{c}_i < 0\}} f_i^*(\mathbf{x}, t)(c_{i,\alpha} - u_\alpha)(c_{i,\beta} - u_\beta) + n_\beta \sum_{i \in \{i | \mathbf{n} \cdot \mathbf{c}_i < 0\}} f_i^*(\mathbf{x}, t)(c_{i,\alpha} + u_\alpha)(c_{i,\beta} + u_\beta) \\
&\quad - n_\beta \sum_{i \in \{i | \mathbf{n} \cdot \mathbf{c}_i > 0\}} f_i^{\text{eq}}(\rho^G, \mathbf{u})(c_{i,\alpha} - u_\alpha)(c_{i,\beta} - u_\beta) - n_\beta \sum_{i \in \{i | \mathbf{n} \cdot \mathbf{c}_i < 0\}} f_i^{\text{eq}}(\rho^G, \mathbf{u})(c_{i,\alpha} + u_\alpha)(c_{i,\beta} + u_\beta) \\
&= -n_\beta \sum_{i \in \{i | \mathbf{n} \cdot \mathbf{c}_i < 0\}} f_i^*(\mathbf{x}, t)(c_{i,\alpha}c_{i,\beta} - c_{i,\alpha}u_\beta - c_{i,\beta}u_\alpha + u_\alpha u_\beta) \\
&\quad + n_\beta \sum_{i \in \{i | \mathbf{n} \cdot \mathbf{c}_i < 0\}} f_i^*(\mathbf{x}, t)(c_{i,\alpha}c_{i,\beta} + c_{i,\alpha}u_\beta + c_{i,\beta}u_\alpha + u_\alpha u_\beta) \\
&\quad - n_\beta \sum_{i \in \{i | \mathbf{n} \cdot \mathbf{c}_i > 0\}} f_i^{\text{eq}}(\rho^G, \mathbf{u})(c_{i,\alpha}c_{i,\beta} - c_{i,\alpha}u_\beta - c_{i,\beta}u_\alpha + u_\alpha u_\beta) \\
&\quad - n_\beta \sum_{i \in \{i | \mathbf{n} \cdot \mathbf{c}_i < 0\}} f_i^{\text{eq}}(\rho^G, \mathbf{u})(c_{i,\alpha}c_{i,\beta} + c_{i,\alpha}u_\beta + c_{i,\beta}u_\alpha + u_\alpha u_\beta) \\
&= 2n_\beta \sum_{i \in \{i | \mathbf{n} \cdot \mathbf{c}_i < 0\}} f_i^*(\mathbf{x}, t)(c_{i,\alpha}u_\beta + c_{i,\beta}u_\alpha) \\
&\quad - n_\beta \sum_{i \in \{i | \mathbf{n} \cdot \mathbf{c}_i > 0\}} f_i^{\text{eq}}(\rho^G, \mathbf{u})(c_{i,\alpha}c_{i,\beta} - c_{i,\alpha}u_\beta - c_{i,\beta}u_\alpha + u_\alpha u_\beta) \\
&\quad - n_\beta \sum_{i \in \{i | \mathbf{n} \cdot \mathbf{c}_i < 0\}} f_i^{\text{eq}}(\rho^G, \mathbf{u})(c_{i,\alpha}c_{i,\beta} + c_{i,\alpha}u_\beta + c_{i,\beta}u_\alpha + u_\alpha u_\beta),
\end{aligned} \tag{A10}$$

The last two sums of the force balance (A10) can be combined by extending with zero, that is, by adding and subtracting $n_\beta f_0^{\text{eq}}(\rho^G, \mathbf{u})(c_{0,\alpha}c_{0,\beta} - c_{0,\alpha}u_\beta - c_{0,\beta}u_\alpha + u_\alpha u_\beta) = n_\beta f_0^{\text{eq}}(\rho^G, \mathbf{u})u_\alpha u_\beta$ so that

$$\begin{aligned}
&-n_\beta \sum_{i \in \{i | \mathbf{n} \cdot \mathbf{c}_i > 0\}} f_i^{\text{eq}}(\rho^G, \mathbf{u})(c_{i,\alpha}c_{i,\beta} - c_{i,\alpha}u_\beta - c_{i,\beta}u_\alpha + u_\alpha u_\beta) - n_\beta \sum_{i \in \{i | \mathbf{n} \cdot \mathbf{c}_i < 0\}} f_i^{\text{eq}}(\rho^G, \mathbf{u})(c_{i,\alpha}c_{i,\beta} + c_{i,\alpha}u_\beta + c_{i,\beta}u_\alpha + u_\alpha u_\beta) \\
&= -n_\beta \sum_{i \in \{i | \mathbf{n} \cdot \mathbf{c}_i \geq 0\}} f_i^{\text{eq}}(\rho^G, \mathbf{u})(c_{i,\alpha}c_{i,\beta} - c_{i,\alpha}u_\beta - c_{i,\beta}u_\alpha + u_\alpha u_\beta) + n_\beta f_0^{\text{eq}}(\rho^G, \mathbf{u})(c_{0,\alpha}c_{0,\beta} - c_{0,\alpha}u_\beta - c_{0,\beta}u_\alpha + u_\alpha u_\beta) \\
&\quad - n_\beta \sum_{i \in \{i | \mathbf{n} \cdot \mathbf{c}_i < 0\}} f_i^{\text{eq}}(\rho^G, \mathbf{u})(c_{i,\alpha}c_{i,\beta} + c_{i,\alpha}u_\beta + c_{i,\beta}u_\alpha + u_\alpha u_\beta) \\
&= -n_\beta \sum_i f_i^{\text{eq}}(\rho^G, \mathbf{u})(c_{i,\alpha}c_{i,\beta} + u_\alpha u_\beta) + n_\beta f_0^{\text{eq}}(\rho^G, \mathbf{u})u_\alpha u_\beta \\
&\quad + n_\beta \sum_{i \in \{i | \mathbf{n} \cdot \mathbf{c}_i \geq 0\}} f_i^{\text{eq}}(\rho^G, \mathbf{u})(c_{i,\alpha}u_\beta + c_{i,\beta}u_\alpha) - n_\beta \sum_{i \in \{i | \mathbf{n} \cdot \mathbf{c}_i < 0\}} f_i^{\text{eq}}(\rho^G, \mathbf{u})(c_{i,\alpha}u_\beta + c_{i,\beta}u_\alpha).
\end{aligned} \tag{A11}$$

Similar as before, the last two sums of the intermediate result (A11) are combined by adding and subtracting $n_\beta \sum_{i \in \{i | \mathbf{n} \cdot \mathbf{c}_i < 0\}} f_i^{\text{eq}}(\rho^G, \mathbf{u})(c_{i,\alpha}u_\beta + c_{i,\beta}u_\alpha)$, which leads to

$$\begin{aligned}
&n_\beta \sum_{i \in \{i | \mathbf{n} \cdot \mathbf{c}_i \geq 0\}} f_i^{\text{eq}}(\rho^G, \mathbf{u})(c_{i,\alpha}u_\beta + c_{i,\beta}u_\alpha) - n_\beta \sum_{i \in \{i | \mathbf{n} \cdot \mathbf{c}_i < 0\}} f_i^{\text{eq}}(\rho^G, \mathbf{u})(c_{i,\alpha}u_\beta + c_{i,\beta}u_\alpha) \\
&= n_\beta \sum_{i \in \{i | \mathbf{n} \cdot \mathbf{c}_i \geq 0\}} f_i^{\text{eq}}(\rho^G, \mathbf{u})(c_{i,\alpha}u_\beta + c_{i,\beta}u_\alpha) + n_\beta \sum_{i \in \{i | \mathbf{n} \cdot \mathbf{c}_i < 0\}} f_i^{\text{eq}}(\rho^G, \mathbf{u})(c_{i,\alpha}u_\beta + c_{i,\beta}u_\alpha) \\
&\quad - 2n_\beta \sum_{i \in \{i | \mathbf{n} \cdot \mathbf{c}_i < 0\}} f_i^{\text{eq}}(\rho^G, \mathbf{u})(c_{i,\alpha}u_\beta + c_{i,\beta}u_\alpha) \\
&= n_\beta \sum_i f_i^{\text{eq}}(\rho^G, \mathbf{u})(c_{i,\alpha}u_\beta + c_{i,\beta}u_\alpha) - 2n_\beta \sum_{i \in \{i | \mathbf{n} \cdot \mathbf{c}_i < 0\}} f_i^{\text{eq}}(\rho^G, \mathbf{u})(c_{i,\alpha}u_\beta + c_{i,\beta}u_\alpha).
\end{aligned} \tag{A12}$$

Combining the transformations (A11) and (A12), and inserting the result in the force balance (A10) gives

$$\begin{aligned}
\frac{F_\alpha}{A} &= 2n_\beta \sum_{i \in \{i | n \cdot c_i < 0\}} \left(f_i^*(\mathbf{x}, t)(c_{i,\alpha}u_\beta + c_{i,\beta}u_\alpha) - f_i^{\text{eq}}(\rho^G, \mathbf{u})(c_{i,\alpha}u_\beta + c_{i,\beta}u_\alpha) \right) + n_\beta f_0^{\text{eq}}(\rho^G, \mathbf{u})(u_\alpha u_\beta) \\
&\quad - n_\beta \sum_i f_i^{\text{eq}}(\rho^G, \mathbf{u})(c_{i,\alpha}c_{i,\beta} - c_{i,\alpha}u_\beta - c_{i,\beta}u_\alpha + u_\alpha u_\beta) \\
&= 2n_\beta \sum_{i \in \{i | n \cdot c_i < 0\}} \left(f_i^*(\mathbf{x}, t) - f_i^{\text{eq}}(\rho^G, \mathbf{u}) \right) (c_{i,\alpha}u_\beta + c_{i,\beta}u_\alpha) + n_\beta f_0^{\text{eq}}(\rho^G, \mathbf{u})(u_\alpha u_\beta) \\
&\quad - n_\beta (\rho^G c_s^2 \delta_{\alpha\beta} + \rho^G u_\alpha u_\beta - \rho^G u_\alpha u_\beta - \rho^G u_\alpha u_\beta + \rho^G u_\alpha u_\beta) \\
&= 2n_\beta \sum_{i \in \{i | n \cdot c_i < 0\}} \left(f_i^*(\mathbf{x}, t) - f_i^{\text{eq}}(\rho^G, \mathbf{u}) \right) (c_{i,\alpha}u_\beta + c_{i,\beta}u_\alpha) + n_\beta f_0^{\text{eq}}(\rho^G, \mathbf{u})(u_\alpha u_\beta) \\
&\quad - n_\alpha p^G,
\end{aligned} \tag{A13}$$

where the equilibrium moments (A8) were used. The expression

$$2n_\beta \sum_{i \in \{i | n \cdot c_i < 0\}} \left(f_i^*(\mathbf{x}, t) - f_i^{\text{eq}}(\rho^G, \mathbf{u}) \right) (c_{i,\alpha}u_\beta + c_{i,\beta}u_\alpha) + n_\beta f_0^{\text{eq}}(\rho^G, \mathbf{u})(u_\alpha u_\beta) \tag{A14}$$

disturbs the force balance at the interface.

A.3 Only missing (OM)

With K and R (30), and the free-surface boundary condition (18), the force balance (24) becomes

$$\begin{aligned}
\frac{F_\alpha}{A} &= -n_\beta \sum_{i \in N^-} f_i^*(\mathbf{x}, t)(c_{i,\alpha} - u_\alpha)(c_{i,\beta} - u_\beta) \\
&\quad - n_\beta \sum_{i \in G^-} \left(f_i^{\text{eq}}(\rho^G, \mathbf{u}) + f_{\bar{i}}^{\text{eq}}(\rho^G, \mathbf{u}) - f_{\bar{i}}^*(\mathbf{x}, t) \right) (c_{i,\alpha} - u_\alpha)(c_{i,\beta} - u_\beta).
\end{aligned} \tag{A15}$$

Using the set relations (31) gives

$$\begin{aligned}
\sum_{i \in G^-} f_{\bar{i}}^*(\mathbf{x}, t)(c_{i,\alpha} - u_\alpha)(c_{i,\beta} - u_\beta) &= \sum_{i \in G^-} f_{\bar{i}}^*(\mathbf{x}, t)(-c_{\bar{i},\alpha} - u_\alpha)(-c_{\bar{i},\beta} - u_\beta) = \\
\sum_{i \in G^-} f_{\bar{i}}^*(\mathbf{x}, t)(c_{\bar{i},\alpha} + u_\alpha)(c_{\bar{i},\beta} + u_\beta) &= \sum_{i \in G^+} f_i^*(\mathbf{x}, t)(c_{i,\alpha} + u_\alpha)(c_{i,\beta} + u_\beta),
\end{aligned} \tag{A16}$$

and analogously

$$\begin{aligned}
\sum_{i \in G^-} f_{\bar{i}}^{\text{eq}}(\rho^G, \mathbf{u})(c_{i,\alpha} - u_\alpha)(c_{i,\beta} - u_\beta) \\
= \sum_{i \in G^+} f_i^{\text{eq}}(\rho^G, \mathbf{u})(c_{i,\alpha} + u_\alpha)(c_{i,\beta} + u_\beta).
\end{aligned} \tag{A17}$$

Inserting the transformations (A16) and (A17) into the force balance (A15) leads to

$$\begin{aligned}
\frac{F_\alpha}{A} &= -n_\beta \sum_{i \in N^-} f_i^*(\mathbf{x}, t)(c_{i,\alpha} - u_\alpha)(c_{i,\beta} - u_\beta) + n_\beta \sum_{i \in G^+} f_i^*(\mathbf{x}, t)(c_{i,\alpha} + u_\alpha)(c_{i,\beta} + u_\beta) \\
&\quad - n_\beta \sum_{i \in G^-} f_i^{\text{eq}}(\rho^G, \mathbf{u})(c_{i,\alpha} - u_\alpha)(c_{i,\beta} - u_\beta) - n_\beta \sum_{i \in G^+} f_i^{\text{eq}}(\rho^G, \mathbf{u})(c_{i,\alpha} + u_\alpha)(c_{i,\beta} + u_\beta).
\end{aligned} \tag{A18}$$

The last two sums of the force balance (A18) are extended with zero by adding and subtracting the term $n_\beta \sum_{i \in G^+} f_i^{\text{eq}}(\rho^G, \mathbf{u})(c_{i,\alpha} u_\beta + c_{i,\beta} u_\alpha)$ giving

$$\begin{aligned}
& -n_\beta \sum_{i \in G^-} f_i^{\text{eq}}(\rho^G, \mathbf{u})(c_{i,\alpha} - u_\alpha)(c_{i,\beta} - u_\beta) - n_\beta \sum_{i \in G^+} f_i^{\text{eq}}(\rho^G, \mathbf{u})(c_{i,\alpha} + u_\alpha)(c_{i,\beta} + u_\beta) \\
& = -n_\beta \sum_{i \in G^-} f_i^{\text{eq}}(\rho^G, \mathbf{u})(c_{i,\alpha} c_{i,\beta} - c_{i,\alpha} u_\beta - c_{i,\beta} u_\alpha + u_\alpha u_\beta) - n_\beta \sum_{i \in G^+} f_i^{\text{eq}}(\rho^G, \mathbf{u})(c_{i,\alpha} c_{i,\beta} + c_{i,\alpha} u_\beta + c_{i,\beta} u_\alpha + u_\alpha u_\beta) \\
& = -n_\beta \sum_{i \in G^- \cup G^+} f_i^{\text{eq}}(\rho^G, \mathbf{u})(c_{i,\alpha} c_{i,\beta} + u_\alpha u_\beta) + n_\beta \sum_{i \in G^-} f_i^{\text{eq}}(\rho^G, \mathbf{u})(c_{i,\alpha} u_\beta + c_{i,\beta} u_\alpha) - n_\beta \sum_{i \in G^+} f_i^{\text{eq}}(\rho^G, \mathbf{u})(c_{i,\alpha} u_\beta + c_{i,\beta} u_\alpha) \\
& = -n_\beta \sum_{i \in G^- \cup G^+} f_i^{\text{eq}}(\rho^G, \mathbf{u})(c_{i,\alpha} c_{i,\beta} + u_\alpha u_\beta) + n_\beta \sum_{i \in G^- \cup G^+} f_i^{\text{eq}}(\rho^G, \mathbf{u})(c_{i,\alpha} u_\beta + c_{i,\beta} u_\alpha) - 2n_\beta \sum_{i \in G^+} f_i^{\text{eq}}(\rho^G, \mathbf{u})(c_{i,\alpha} u_\beta + c_{i,\beta} u_\alpha) \\
& = -n_\beta \sum_{i \in G^- \cup G^+} f_i^{\text{eq}}(\rho^G, \mathbf{u})(c_{i,\alpha} c_{i,\beta} + u_\alpha u_\beta - c_{i,\alpha} u_\beta - c_{i,\beta} u_\alpha) - 2n_\beta \sum_{i \in G^+} f_i^{\text{eq}}(\rho^G, \mathbf{u})(c_{i,\alpha} u_\beta + c_{i,\beta} u_\alpha).
\end{aligned} \tag{A19}$$

The intermediate result (A19) is again extended by subtracting and adding the term $n_\beta \sum_{i \in T \setminus (G^- \cup G^+)} f_i^{\text{eq}}(\rho^G, \mathbf{u})(c_{i,\alpha} c_{i,\beta} + u_\alpha u_\beta - c_{i,\alpha} u_\beta - c_{i,\beta} u_\alpha)$ to obtain

$$\begin{aligned}
& -n_\beta \sum_{i \in G^- \cup G^+} f_i^{\text{eq}}(\rho^G, \mathbf{u})(c_{i,\alpha} c_{i,\beta} + u_\alpha u_\beta - c_{i,\alpha} u_\beta - c_{i,\beta} u_\alpha) - 2n_\beta \sum_{i \in G^+} f_i^{\text{eq}}(\rho^G, \mathbf{u})(c_{i,\alpha} u_\beta + c_{i,\beta} u_\alpha) \\
& = -n_\beta \sum_{i \in T} f_i^{\text{eq}}(\rho^G, \mathbf{u})(c_{i,\alpha} c_{i,\beta} + u_\alpha u_\beta - c_{i,\alpha} u_\beta - c_{i,\beta} u_\alpha) + n_\beta \sum_{i \in T \setminus (G^- \cup G^+)} f_i^{\text{eq}}(\rho^G, \mathbf{u})(c_{i,\alpha} c_{i,\beta} + u_\alpha u_\beta - c_{i,\alpha} u_\beta - c_{i,\beta} u_\alpha) \\
& \quad - 2n_\beta \sum_{i \in G^+} f_i^{\text{eq}}(\rho^G, \mathbf{u})(c_{i,\alpha} u_\beta + c_{i,\beta} u_\alpha),
\end{aligned} \tag{A20}$$

which can be rewritten using the the equilibrium moments (A8) as

$$\begin{aligned}
& -n_\beta \sum_{i \in T} f_i^{\text{eq}}(\rho^G, \mathbf{u})(c_{i,\alpha} c_{i,\beta} + u_\alpha u_\beta - c_{i,\alpha} u_\beta - c_{i,\beta} u_\alpha) + n_\beta \sum_{i \in T \setminus (G^- \cup G^+)} f_i^{\text{eq}}(\rho^G, \mathbf{u})(c_{i,\alpha} c_{i,\beta} + u_\alpha u_\beta - c_{i,\alpha} u_\beta - c_{i,\beta} u_\alpha) \\
& \quad - 2n_\beta \sum_{i \in G^+} f_i^{\text{eq}}(\rho^G, \mathbf{u})(c_{i,\alpha} u_\beta + c_{i,\beta} u_\alpha) \\
& = -n_\beta (\rho^G c_s^2 \delta_{\alpha\beta} + \rho^G u_\alpha u_\beta + \rho^G u_\alpha u_\beta - \rho^G u_\alpha u_\beta - \rho^G u_\alpha u_\beta) + n_\beta \sum_{i \in T \setminus (G^- \cup G^+)} f_i^{\text{eq}}(\rho^G, \mathbf{u})(c_{i,\alpha} c_{i,\beta} + u_\alpha u_\beta - c_{i,\alpha} u_\beta - c_{i,\beta} u_\alpha) \\
& \quad - 2n_\beta \sum_{i \in G^+} f_i^{\text{eq}}(\rho^G, \mathbf{u})(c_{i,\alpha} u_\beta + c_{i,\beta} u_\alpha).
\end{aligned} \tag{A21}$$

Inserting the transformation (A21) into the force balance (A18) gives

$$\begin{aligned}
\frac{F_\alpha}{A} & = -n_\beta \sum_{i \in N^-} f_i^*(\mathbf{x}, t)(c_{i,\alpha} c_{i,\beta} - c_{i,\alpha} u_\beta - c_{i,\beta} u_\alpha + u_\alpha u_\beta) + n_\beta \sum_{i \in G^+} f_i^*(\mathbf{x}, t)(c_{i,\alpha} c_{i,\beta} + c_{i,\alpha} u_\beta + c_{i,\beta} u_\alpha + u_\alpha u_\beta) \\
& \quad + n_\beta \sum_{i \in T \setminus (G^- \cup G^+)} f_i^{\text{eq}}(\rho^G, \mathbf{u})(c_{i,\alpha} c_{i,\beta} + u_\alpha u_\beta - c_{i,\alpha} u_\beta - c_{i,\beta} u_\alpha) - 2n_\beta \sum_{i \in G^+} f_i^{\text{eq}}(\rho^G, \mathbf{u})(c_{i,\alpha} u_\beta + c_{i,\beta} u_\alpha) \\
& \quad - n_\beta \rho^G c_s^2 \delta_{\alpha\beta} \\
& = -n_\beta \sum_{i \in N^-} f_i^*(\mathbf{x}, t)(c_{i,\alpha} c_{i,\beta} - c_{i,\alpha} u_\beta - c_{i,\beta} u_\alpha + u_\alpha u_\beta) + n_\beta \sum_{i \in G^+} f_i^*(\mathbf{x}, t)(c_{i,\alpha} c_{i,\beta} + c_{i,\alpha} u_\beta + c_{i,\beta} u_\alpha + u_\alpha u_\beta) \\
& \quad + n_\beta \sum_{i \in T \setminus (G^- \cup G^+)} f_i^{\text{eq}}(\rho^G, \mathbf{u})(c_{i,\alpha} c_{i,\beta} - c_{i,\alpha} u_\beta - c_{i,\beta} u_\alpha + u_\alpha u_\beta) - 2n_\beta \sum_{i \in G^+} f_i^{\text{eq}}(\rho^G, \mathbf{u})(c_{i,\alpha} u_\beta + c_{i,\beta} u_\alpha) \\
& \quad - n_\alpha p^G,
\end{aligned} \tag{A22}$$

where the balance of the forces is disturbed by

$$\begin{aligned}
& -n_\beta \sum_{i \in N^-} f_i^*(\mathbf{x}, t)(c_{i,\alpha} c_{i,\beta} - c_{i,\alpha} u_\beta - c_{i,\beta} u_\alpha + u_\alpha u_\beta) + n_\beta \sum_{i \in G^+} f_i^*(\mathbf{x}, t)(c_{i,\alpha} c_{i,\beta} + c_{i,\alpha} u_\beta + c_{i,\beta} u_\alpha + u_\alpha u_\beta) \\
& \quad + n_\beta \sum_{i \in T \setminus (G^- \cup G^+)} f_i^{\text{eq}}(\rho^G, \mathbf{u})(c_{i,\alpha} c_{i,\beta} - c_{i,\alpha} u_\beta - c_{i,\beta} u_\alpha + u_\alpha u_\beta) - 2n_\beta \sum_{i \in G^+} f_i^{\text{eq}}(\rho^G, \mathbf{u})(c_{i,\alpha} u_\beta + c_{i,\beta} u_\alpha).
\end{aligned} \tag{A23}$$

B NUMERICAL EXPERIMENTS

This section extends Section 4 with additional results and figures.

B.1 Gravity wave

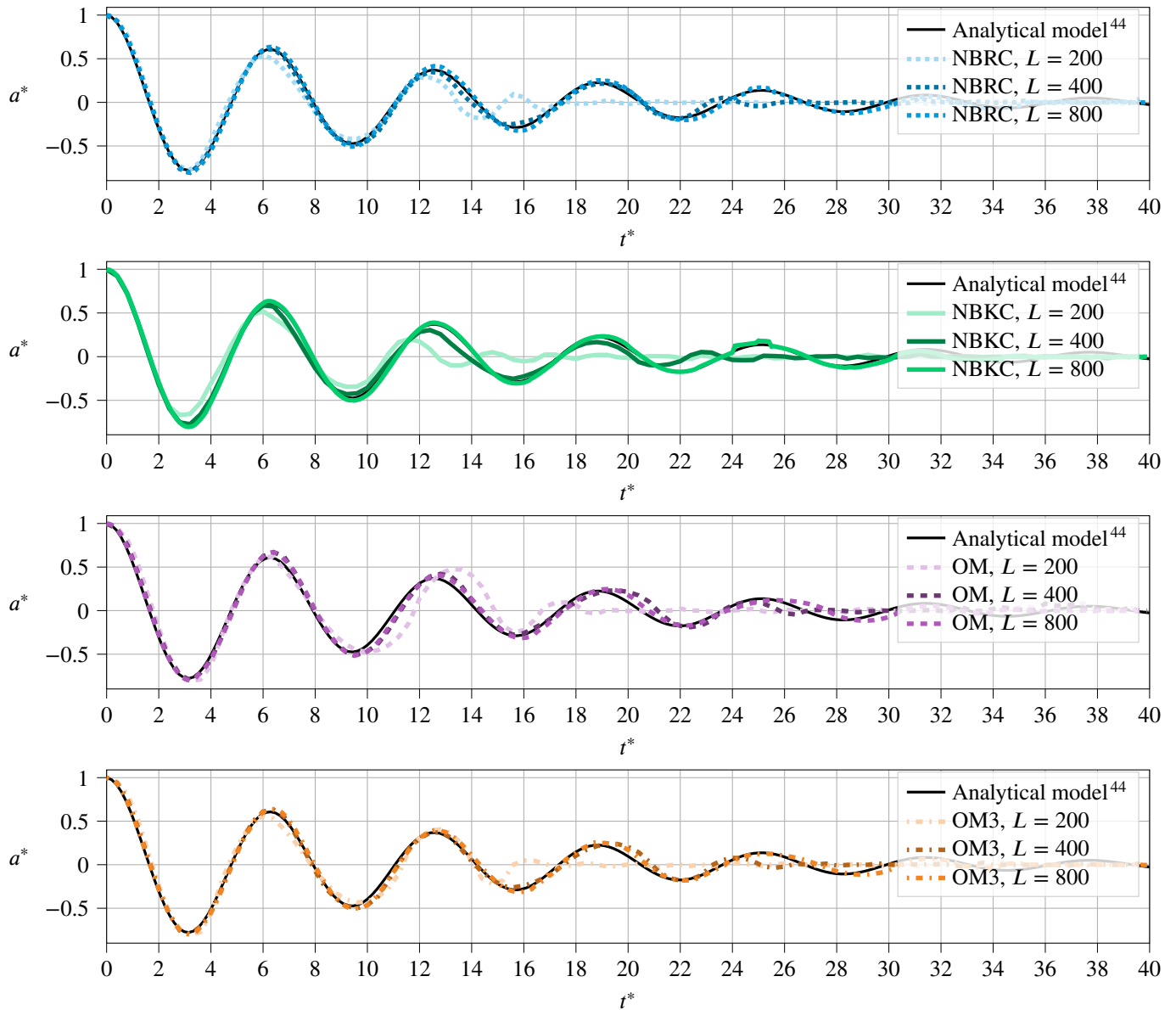


FIGURE B1 Simulated surface elevation of the gravity wave in terms of non-dimensional amplitude $a^*(0, t^*)$ and time t^* . The simulations were performed with computational domain resolutions, that is, wavelengths of $L \in \{200, 400, 800\}$ lattice cells. A higher computational domain resolution captures more of the standing wave's oscillations.

B.2 Rectangular dam break

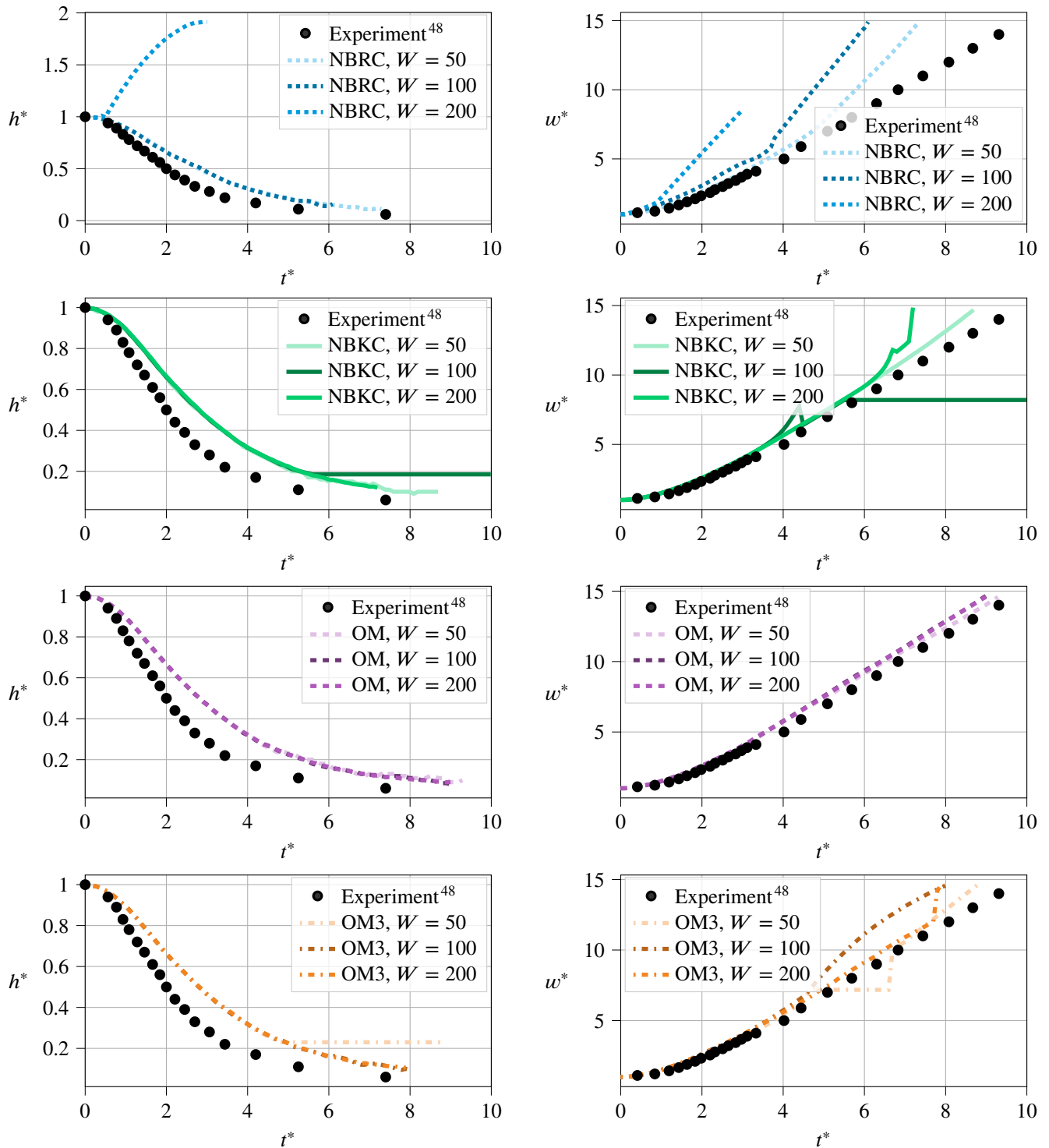


FIGURE B2 Simulated rectangular dam break with non-dimensionalized residual dam height $h^*(t^*)$, width $w^*(t^*)$, and time t^* . The simulations were performed with computational domain resolutions, that is, initial dam widths of $W \in \{50, 100, 200\}$ lattice cells. Only the OM variant converged well. The other variants led to splashing as described in Section 4.2.2. These splash droplets disturbed the evaluation algorithm and even led to numerical instabilities as observed for the NBKC variant with $W = 100$.

B.3 Cylindrical dam break

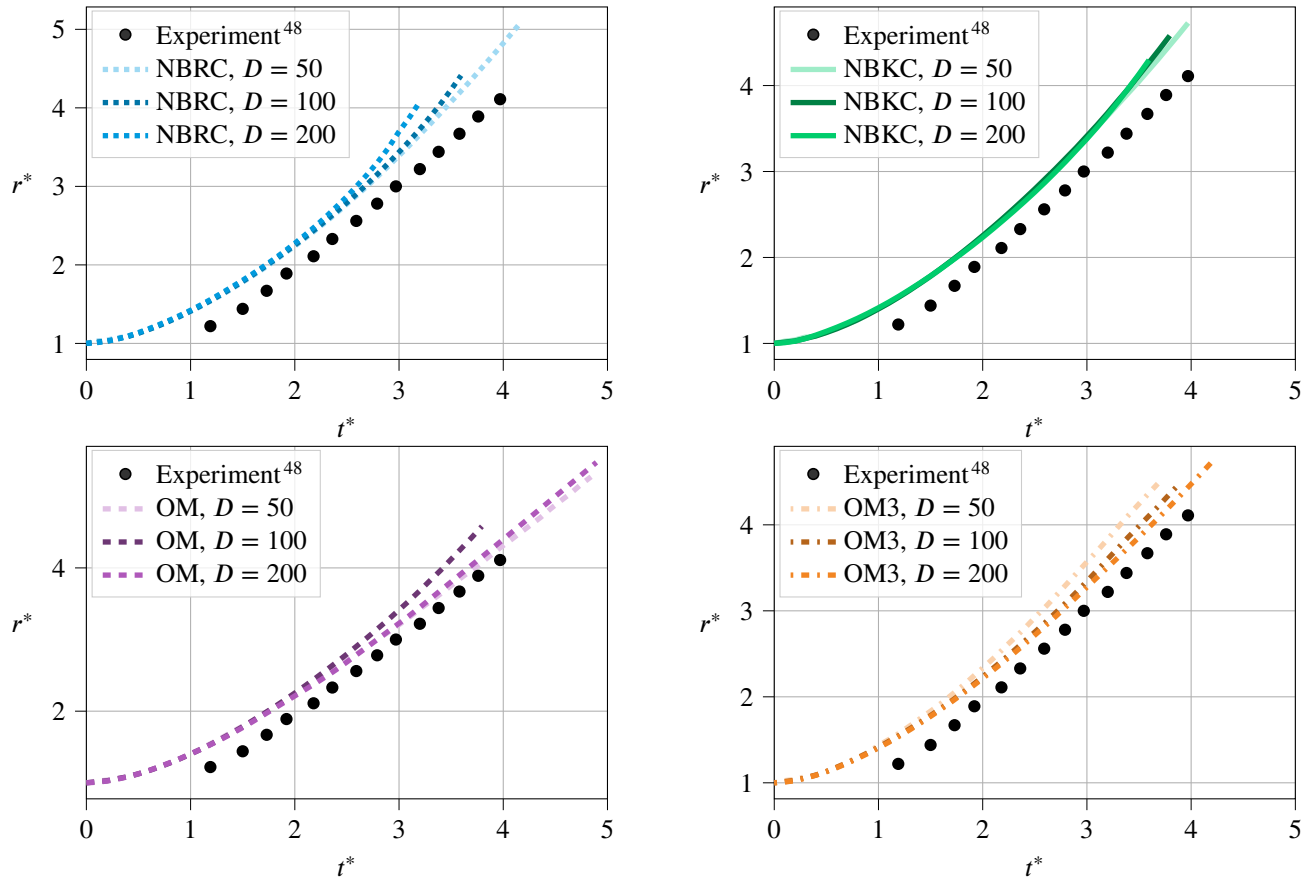


FIGURE B3 Simulated cylindrical dam break with non-dimensionalized liquid column radius $r^*(t^*)$ and time t^* . The simulations were performed with computational domain resolutions, that is, initial column diameters of $D \in \{50, 100, 200\}$ lattice cells. The markers represent the mean values of $r^*(t^*)$. All variants but the NBRC converged well.

B.4 Taylor bubble

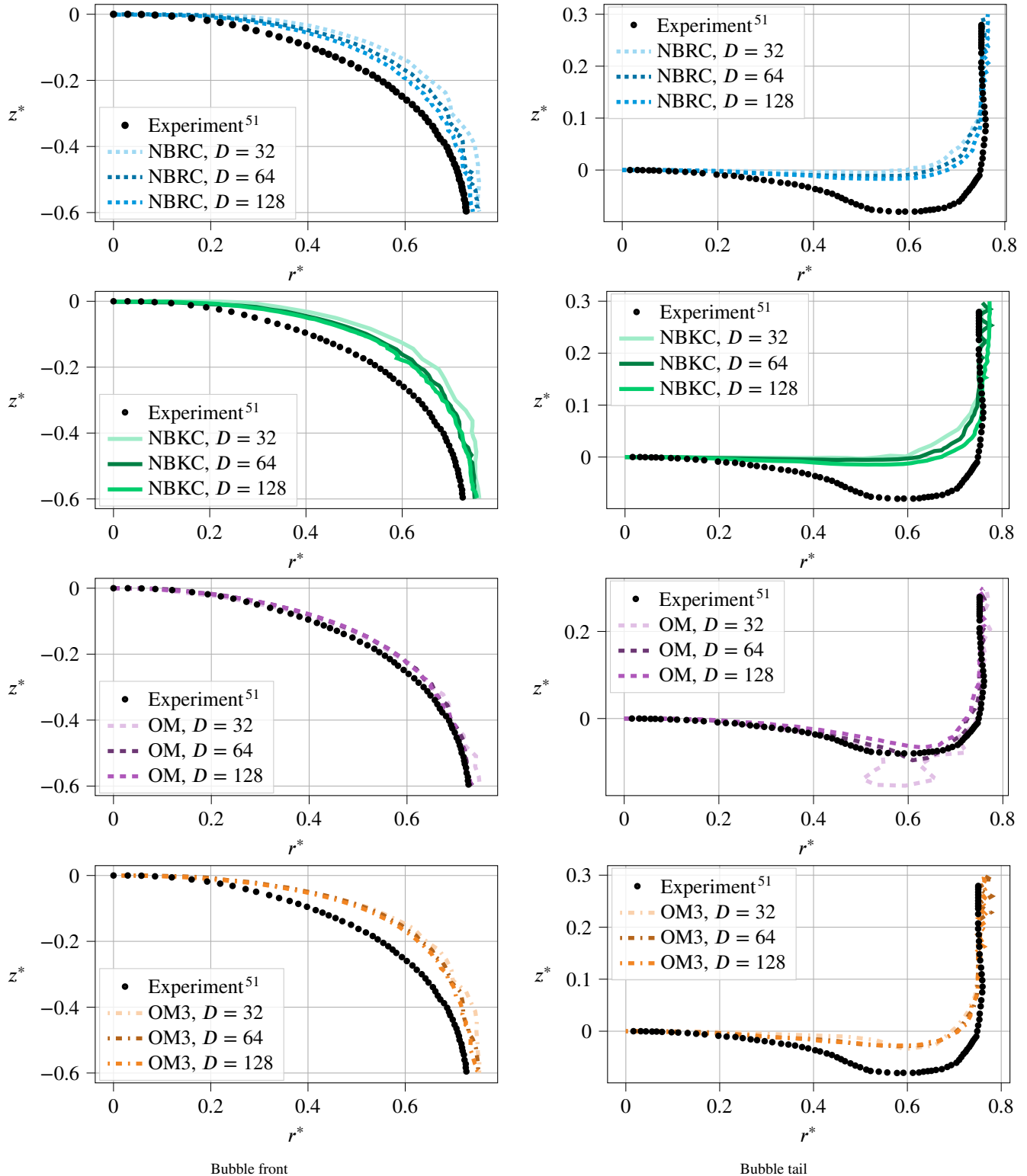


FIGURE B4 Simulated shape of the Taylor bubble's front and tail. The simulations were performed with computational domain resolutions, that is, tube diameters of $D \in \{32, 64, 128\}$ lattice cells. The comparison with experimental data⁵¹ was drawn in terms of the non-dimensionalized axial location z^* and radial location r^* at time $t^* = 15$. All boundary condition variants converged well.

References

1. Körner C, Thies M, Hofmann T, Thürey N, Rüde U. Lattice Boltzmann Model for Free Surface Flow for Modeling Foaming. *Journal of Statistical Physics* 2005; 121(1): 179–196. doi: 10.1007/s10955-005-8879-8
2. Scardovelli R, Zaleski S. Direct Numerical Simulation of Free-Surface and Interfacial Flow. *Annual Review of Fluid Mechanics* 1999; 31(1): 567–603. doi: 10.1146/annurev.fluid.31.1.567
3. Hirt C, Nichols B. Volume of Fluid (VOF) Method for the Dynamics of Free Boundaries. *Journal of Computational Physics* 1981; 39(1). doi: 10.1016/0021-9991(81)90145-5
4. Donath S, Mecke K, Rabha S, Buwa V, Rüde U. Verification of Surface Tension in the Parallel Free Surface Lattice Boltzmann Method in waLberla. *Computers & Fluids* 2011; 45(1). doi: 10.1016/j.compfluid.2010.12.027
5. Zhao Z, Huang P, Li Y, Li J. A Lattice Boltzmann Method for Viscous Free Surface Waves in Two Dimensions. *International Journal for Numerical Methods in Fluids* 2013; 71(2): 223–248. doi: 10.1002/flid.3660
6. Janßen C, Krafczyk M. Free Surface Flow Simulations on GPGPUs Using the LBM. *Computers & Mathematics with Applications* 2011; 61(12). doi: 10.1016/j.camwa.2011.03.016
7. Lehmann M, Oehlschlägel LM, Häusl FP, Held A, Gekle S. Ejection of Marine Microplastics by Raindrops: A Computational and Experimental Study. *Microplastics and Nanoplastics* 2021; 1(1). doi: 10.1186/s43591-021-00018-8
8. Ammer R, Markl M, Ljungblad U, Körner C, Rüde U. Simulating Fast Electron Beam Melting with a Parallel Thermal Free Surface Lattice Boltzmann Method. *Computers & Mathematics with Applications* 2014; 67(2). doi: 10.1016/j.camwa.2013.10.001
9. Becker J, Junk M, Kehrwald D, Thömmes G, Yang Z. A Combined Lattice BGK/Level Set Method for Immiscible Two-Phase Flows. *Computers & Mathematics with Applications* 2009; 58(5). doi: 10.1016/j.camwa.2009.02.005
10. Lallemand P, Luo LS, Peng Y. A Lattice Boltzmann Front-Tracking Method for Interface Dynamics with Surface Tension in Two Dimensions. *Journal of Computational Physics* 2007; 226(2). doi: 10.1016/j.jcp.2007.05.021
11. Gunstensen AK, Rothman DH, Zaleski S, Zanetti G. Lattice Boltzmann Model of Immiscible Fluids. *Physical Review A* 1991; 43(8). doi: 10.1103/PhysRevA.43.4320
12. Inamuro T, Ogata T, Tajima S, Konishi N. A Lattice Boltzmann Method for Incompressible Two-Phase Flows with Large Density Differences. *Journal of Computational Physics* 2004; 198(2). doi: 10.1016/j.jcp.2004.01.019
13. Zheng HW, Shu C, Chew YT. Lattice Boltzmann Interface Capturing Method for Incompressible Flows. *Physical Review E* 2005; 72(5). doi: 10.1103/PhysRevE.72.056705
14. Fakhari A, Mitchell T, Leonardi C, Bolster D. Improved Locality of the Phase-Field Lattice-Boltzmann Model for Immiscible Fluids at High Density Ratios. *Physical Review E* 2017; 96(5). doi: 10.1103/PhysRevE.96.053301
15. Swift MR, Osborn WR, Yeomans JM. Lattice Boltzmann Simulation of Nonideal Fluids. *Physical Review Letters* 1995; 75(5). doi: 10.1103/PhysRevLett.75.830
16. Shan X, Chen H. Simulation of Nonideal Gases and Liquid-Gas Phase Transitions by the Lattice Boltzmann Equation. *Physical Review E* 1994; 49(4). doi: 10.1103/PhysRevE.49.2941
17. Schwarzmeier C, Holzer M, Mitchell T, Lehmann M, Häusl F, Rüde U. Comparison of Free-Surface and Conservative Allen–Cahn Phase-Field Lattice Boltzmann Method. *Journal of Computational Physics* 2023; 473: 111753. doi: 10.1016/j.jcp.2022.111753
18. Bogner S, Rüde U, Harting J. Curvature Estimation from a Volume-of-Fluid Indicator Function for the Simulation of Surface Tension and Wetting with a Free-Surface Lattice Boltzmann Method. *Physical Review E* 2016; 93(4). doi: 10.1103/PhysRevE.93.043302

19. Bogner S. *Direct Numerical Simulation of Liquid-Gas-Solid Flows Based on the Lattice Boltzmann Method*. PhD thesis. Friedrich-Alexander-Universität Erlangen-Nürnberg, Erlangen; 2017.
20. Thies M. *Lattice Boltzmann Modeling with Free Surfaces Applied to Formation of Metal Foams*. PhD thesis. Universität Erlangen-Nürnberg, Erlangen; 2005.
21. Bauer M, Eibl S, Godenschwager C, et al. waLBerla: A Block-Structured High-Performance Framework for Multiphysics Simulations. *Computers & Mathematics with Applications* 2021; 81. doi: 10.1016/j.camwa.2020.01.007
22. Schwarzmeier C, Rüde U. Comparison of Refilling Schemes in the Free-Surface Lattice Boltzmann Method. *AIP Advances* 2022; 12(11): 23. doi: 10.1063/5.0131159
23. Krüger T, Kusumaatmaja H, Kuzmin A, Shardt O, Silva G, Viggen EM. *The Lattice Boltzmann Method: Principles and Practice*. Switzerland: Springer . 2017.
24. Bauer M, Silva G, Rüde U. Truncation Errors of the D3Q19 Lattice Model for the Lattice Boltzmann Method. *Journal of Computational Physics* 2020; 405(C). doi: 10.1016/j.jcp.2019.109111
25. Guo Z, Zheng C, Shi B. Discrete Lattice Effects on the Forcing Term in the Lattice Boltzmann Method. *Physical Review E* 2002; 65(4). doi: 10.1103/PhysRevE.65.046308
26. Hou S, Sterling J, Chen S, Doolen GD. A Lattice Boltzmann Subgrid Model for High Reynolds Number Flows. In: Lawniczak AT, Kapral R., eds. *Pattern Formation and Lattice Gas Automata*. 6 of *Fields Institute Communications*. American Mathematical Society. ; 1996
27. Yu H, Girimaji SS, Luo LS. DNS and LES of Decaying Isotropic Turbulence with and without Frame Rotation Using Lattice Boltzmann Method. *Journal of Computational Physics* 2005; 209(2). doi: 10.1016/j.jcp.2005.03.022
28. Pohl T. *High Performance Simulation of Free Surface Flows Using the Lattice Boltzmann Method*. PhD thesis. Universität Erlangen-Nürnberg, Erlangen; 2008.
29. Thürey N. *Physically Based Animation of Free Surface Flows with the Lattice Boltzmann Method*. PhD thesis. Universität Erlangen-Nürnberg, Erlangen; 2007.
30. Donath S. *Wetting Models for a Parallel High-Performance Free Surface Lattice Boltzmann Method*. PhD thesis. Universität Erlangen-Nürnberg, Erlangen; 2011.
31. Bogner S, Ammer R, Rüde U. Boundary Conditions for Free Interfaces with the Lattice Boltzmann Method. *Journal of Computational Physics* 2015; 297. doi: 10.1016/j.jcp.2015.04.055
32. Parker BJ, Youngs DL. Two and Three Dimensional Eulerian Simulation and Fluid Flow with Material Interfaces. technical Report 01/92, UK Atomic Weapons Establishment; ; 1992.
33. Williams MW, Kothe DB, Puckett EG. Accuracy and Convergence of Continuum Surface Tension Models. In: Shyy W, Narayanan R., eds. *Fluid Dynamics at Interfaces* Cambridge University Press. first ed. 1999 (pp. 294–305).
34. Anderl D, Bogner S, Rauh C, Rüde U, Delgado A. Free Surface Lattice Boltzmann with Enhanced Bubble Model. *Computers & Mathematics with Applications* 2014; 67(2). doi: 10.1016/j.camwa.2013.06.007
35. Ladd AJC. Numerical Simulations of Particulate Suspensions via a Discretized Boltzmann Equation. Part 2. Numerical Results. *Journal of Fluid Mechanics* 1994; 271. doi: 10.1017/S0022112094001783
36. Ladd AJC. Numerical Simulations of Particulate Suspensions via a Discretized Boltzmann Equation. Part 1. Theoretical Foundation. *Journal of Fluid Mechanics* 1994; 271. doi: 10.1017/S0022112094001771
37. Thorimbert Y, Chopard B, Lätt J. Implementation of Lattice Boltzmann Free-Surface and Shallow Water Models and Their Two-Way Coupling. *MethodsX* 2021; 8: 101338. doi: 10.1016/j.mex.2021.101338
38. Biscarini C, Di Francesco S, Mencattini M. Application of the Lattice Boltzmann Method for Large-scale Hydraulic Problems. *International Journal of Numerical Methods for Heat & Fluid Flow* 2011; 21(5): 584–601. doi: 10.1108/09615531111135846

39. Cubeddu A, Rauh C, Ulrich V. Simulations of Bubble Growth and Interaction in High Viscous Fluids Using the Lattice Boltzmann Method. *International Journal of Multiphase Flow* 2017; 93: 108–114. doi: 10.1016/j.ijmultiphaseflow.2017.04.001
40. Zhao P, Li Q, Kuang SB, Zou Z. LBM-LES Simulation of the Transient Asymmetric Flow and Free Surface Fluctuations under Steady Operating Conditions of Slab Continuous Casting Process. *Metallurgical and Materials Transactions B* 2017; 48(1): 456–470. doi: 10.1007/s11663-016-0830-7
41. Chiappini D, Di Ilio G, Bella G. Analysis of the Fluid Motion Induced by a Vibrating Lamina Through Free Surface-Lattice Boltzmann Coupled Method. In: ASME. American Society of Mechanical Engineers; 2018; Pittsburgh, Pennsylvania, USA: V009T12A003
42. Bublík O, Lobovský L, Heidler V, Mandys T, Vimmr J. Experimental Validation of Numerical Simulations of Free-Surface Flow within Casting Mould Cavities. *Engineering Computations* 2021; 38(10): 4024–4046. doi: 10.1108/EC-08-2020-0458
43. Huang Z, Diao W, Wu J, Cheng Y, Huai W. Three-Dimensional Simulation of Reservoir Temperature and Pollutant Transport by the Lattice Boltzmann Method. *Environmental Science and Pollution Research* 2021; 28(1): 459–472. doi: 10.1007/s11356-020-10174-8
44. Dingemans MW. *Water Wave Propagation Over Uneven Bottoms: Part 1*. 13 of *Advanced Series on Ocean Engineering*. World Scientific Publishing Company . 1997
45. Lamb H. *Hydrodynamics*. Cambridge University Press. sixth ed. 1975.
46. Sato K, Kawasaki K, Koshimura S. A Comparative Study of the Cumulant Lattice Boltzmann Method in a Single-Phase Free-Surface Model of Violent Flows. *Computers & Fluids* 2022; 236. doi: 10.1016/j.compfluid.2021.105303
47. Moraga NO, Lemus LA, Saavedra MA, Lemus-Mondaca RA. VOF/FVM Prediction and Experimental Validation for Shear-Thinning Fluid Column Collapse. *Computers & Mathematics with Applications* 2015; 69(2). doi: 10.1016/j.camwa.2014.11.018
48. Martin JC, Moyce WJ, Penney WG, Price AT, Thornhill CK. Part IV. An Experimental Study of the Collapse of Liquid Columns on a Rigid Horizontal Plane. *Philosophical Transactions of the Royal Society of London. Series A, Mathematical and Physical Sciences* 1952; 244(882). doi: 10.1098/rsta.1952.0006
49. Rumble J., ed. *CRC Handbook of Chemistry and Physics*. CRC Press. one hundred second ed. 2021.
50. Pavlidis T. *Algorithms for Graphics and Image Processing*. Berlin, Heidelberg: Springer Berlin Heidelberg . 1982
51. Bugg J, Saad G. The Velocity Field around a Taylor Bubble Rising in a Stagnant Viscous Fluid: Numerical and Experimental Results. *International Journal of Multiphase Flow* 2002; 28(5). doi: 10.1016/S0301-9322(02)00002-2
52. Wang AB, Chen CC. Splashing Impact of a Single Drop onto Very Thin Liquid Films. *Physics of Fluids* 2000; 12(9). doi: 10.1063/1.1287511